

Article

Thermoacoustic Combustion Stability Analysis of a Bluff Body-Stabilized Burner Fueled by Methane–Air and Hydrogen–Air Mixtures

Vito Ceglie ^{1,*} , Michele Stefanizzi ¹ , Tommaso Capurso ² , Francesco Fornarelli ^{3,4} 
and Sergio M. Camporeale ¹ 

¹ Department of Mechanics, Mathematics & Management, Polytechnic University of Bari, Via Orabona 4, 70125 Bari, Italy

² Arts et Metiers Institute of Technology, 151 Bd de l'Hôpital, 75013 Paris, France

³ Department of Sciences of Agriculture, Food, Natural Resources and Engineering, University of Foggia, Via Napoli 25, 71121 Foggia, Italy

⁴ National Group of Mathematical Physics (GNFM) of the Italian National Institute of High Mathematics (INDAM), Piazzale Aldo Moro, 5, 00185 Rome, Italy

* Correspondence: vito.ceglie@poliba.it

Abstract: Hydrogen can play a key role in the gradual transition towards a full decarbonization of the combustion sector, e.g., in power generation. Despite the advantages related to the use of this carbon-free fuel, there are still several challenging technical issues that must be addressed such as the thermoacoustic instability triggered by hydrogen. Given that burners are usually designed to work with methane or other fossil fuels, it is important to investigate their thermoacoustic behavior when fueled by hydrogen. In this framework, the present work aims to propose a methodology which combines Computational Fluid Dynamics CFD (3D Reynolds-Averaged Navier-Stokes (RANS)) and Finite Element Method (FEM) approaches in order to investigate the fluid dynamic and the thermoacoustic behavior introduced by hydrogen in a burner (a lab-scale bluff body stabilized burner) designed to work with methane. The case of CH₄-air mixture was used for the validation against experimental results and benchmark CFD data available in the literature. Numerical results obtained from CFD simulations, namely thermofluidodynamic properties and flame characteristics (i.e., time delay and heat release rate) are used to evaluate the effects of the fuel change on the Flame Response Function to the acoustic perturbation by means of a FEM approach. As results, in the H₂-air mixture case, the time delay decreases and heat release rate increases with respect to the CH₄-air mixture. A study on the Rayleigh index was carried out in order to analyze the influence of H₂-air mixture on thermoacoustic instability of the burner. Finally, an analysis of both frequency and growth rate (GR) on the first four modes was carried out by comparing the two mixtures. In the H₂-air case the modes are prone to become more unstable with respect to the same modes of the case fueled by CH₄-air, due to the change in flame topology and variation of the heat release rate and time delay fields.

Keywords: hydrogen; combustion; thermoacoustic; Helmholtz solver; CFD; Flame Response Function



Citation: Ceglie, V.; Stefanizzi, M.; Capurso, T.; Fornarelli, F.; Camporeale, S.M. Thermoacoustic Combustion Stability Analysis of a Bluff Body-Stabilized Burner Fueled by Methane–Air and Hydrogen–Air Mixtures. *Energies* **2023**, *16*, 3272. <https://doi.org/10.3390/en16073272>

Academic Editors: Theodoros Zannis, Apostolos Pesyridis, Dimitrios Kyritsis, Elias Yfantis and Ioannis Roumeliotis

Received: 8 March 2023

Revised: 27 March 2023

Accepted: 30 March 2023

Published: 6 April 2023



Copyright: © 2023 by the authors. Licensee MDPI, Basel, Switzerland. This article is an open access article distributed under the terms and conditions of the Creative Commons Attribution (CC BY) license (<https://creativecommons.org/licenses/by/4.0/>).

1. Introduction

Hydrogen, being a carbon-free fuel, can play an important role in the current global decarbonization process in the power generation sector [1–3]. The power generation sector is mainly based on combustion technologies, predominantly with gas turbines. Therefore, it is necessary for academia and industry to make this field more sustainable, often defined as one of the hardest-to-abate sectors. Hydrogen can play a key role in gas turbine technology in the gradual transition towards full decarbonization of the combustion field. On this topic, Stefanizzi et al. [4] presented a review of modern combustion strategies in gas turbines for aviation and power production, with an emphasis on specific elements relating to next-gen

fuels, burners, and combustion procedures. Griebel [5] presented modern gas turbine technologies, and explored combustion basics pertinent to gas turbines operating with hydrogen-rich fuels. In this framework, gas turbines fueled by hydrogen or hydrogen–methane blends would permit a significant long-term reduction in emissions [6,7]. The technical literature presents several studies (both experimental and numerical) which investigate the effects of hydrogen on the behavior of gas turbine combustors. For instance, Guiberti et al. [8] carried out experimental studies on premixed combustion in a gas turbine burner fueled by a methane–hydrogen mixture in order to evaluate the influence of hydrogen on stabilizing an M-flame (flame shape in which combustion takes place between the outer and inner recirculation zone). According to the experimental investigations on the PRECCINSTA burner [9] carried out by Chterevev et al. [10,11], hydrogen enrichment influences flame topology, highlighting the transition from an M- to V-shaped flame. Schefer et al. [12] drew attention to the variation in flame structure and the increase in the OH peak concentration due to the addition of hydrogen in a methane–air mixture in a premixed swirl-stabilized flame.

An important aspect to consider is related to the fact that hydrogen enrichment in gas turbine burners can lead to the displacement of combustion instabilities. Combustion instability is a physical phenomenon that occurs during the combustion process due to the interaction between acoustic waves propagating inside the combustion chamber and thermal release fluctuations. Thermoacoustic instability is mainly investigated by means of three approaches, which are based on: low-order numerical models [13–15], CFD (Computational Fluid Dynamics) models [16–20], and Helmholtz solver models (FEM) [21–24]. In details, low-order models divide the thermoacoustic system into a network of elementary acoustic domains (e.g., pipes, burner, flame, etc.), where the acoustic field is represented as a solution to the Helmholtz equation. The CFD models (e.g., solving RANS, URANS, and LES approaches) allow the analysis of the thermo-fluid dynamic flow fields inside the combustor, in a more realistic configuration; however, this requires high computational costs. FEM models are used to transform time domain-based differential equation problems into eigenvalue problems in the frequency domain by using the Fourier transform.

In the last decades many research groups have devoted significant efforts to studying this phenomenon by means of experimental and numerical approaches (mainly based on CFD and low-order models) [22,25–27]. For instance, an exhaustive review on the influence of hydrogen and hydrogen-enriched natural gas on the thermoacoustic instability was carried out by Beita et al. [28]. Janus et al. [29] investigated a sub-scale combustor fueled by natural gas, propane, and some hydrogen–hydrocarbon mixtures. Numerical and experimental results highlighted that the shift in instability is primarily due to the change in reaction rate. Æsøy et al. [30] scaled the flame transfer function (FTF) of an M-flame on a non-swirled bluff body-stabilized burner fueled by different hydrogen and methane blends. Aguilar et al. [31] used scaled distributed time lag in order to predict the linear stability limit by means a low-order network model on a perfectly premixed combustor fueled by several methane–hydrogen blends. The measurements of bulk velocity and flame length were enough in order to predict the flame transfer function (FTF). The shape of the flame changes in function of hydrogen quantity in the blend. The increase in hydrogen in the blend led to a decrease in the characteristic flame length. Shanbhogue et al. [32] proved that the critical equivalence ratio, that indicates the transition between stability and instability of a swirl-stabilized combustor burning at atmospheric pressure and temperature, decreases when using methane–hydrogen mixtures. The influence of the equivalence ratio on the azimuthal instabilities of an annular laboratory-scale burner fueled by methane–hydrogen mixtures was studied by Ahn et al. [33]. López et al. [34] studied the thermoacoustic instabilities of lean hydrogen–air premixed flames in a quasi-2D geometry, highlighting the importance of the equivalence ratio and the role of channel thickness. Jin Kim et al. [35] observed using dynamic pressure sensors and OH planar laser-induced fluorescence (OH PLIF), the multi-mode combustion instabilities in GE7EA combustor fueled by mixture enriched with hydrogen by means of a partial premixed flame that can restrict flashback.

FEM simulations based on Helmholtz solvers with respect to low-order models offer the possibility to account for the actual geometry of the burner with the fluid-dynamic properties obtained by CFD simulation. Indeed, the FEM approach requires information on the heat release, time delay, flow field, pressure, and temperature distribution, in order to correctly model instabilities during the combustion process. For this reason, appropriate CFD simulations are needed to investigate the combustion process and to provide the information required by the FEM models. Therefore, it is interesting to combine CFD with FEM approaches in order to investigate the thermoacoustic behavior of a burner fueled by hydrogen–air mixture. In detail, the lab-scale bluff body stabilized premixed burner studied at the Vanderbilt University has been investigated by means of a fully 3D RANS approach. The choice of this burner fueled by methane–air mixture is due to the presence of many numerical and experimental studies in the literature. Indeed, Pan et al. [36] performed an experimental study that highlighted the influence of the blockage ratio, turbulence intensity, value of the vertex angle, and equivalence ratio on the recirculation zone after the bluff body. In addition, Nandula et al. [37] experimentally characterized this burner. Regarding numerical investigations, Cannon et al. [38] used an “in situ tabulation method”, with a five-step mechanism as a chemical model in order to predict the behaviour of the aforementioned burner. Andreini et al. [39] compared LES and RANS simulations on this burner by using the OpenFoam[®] and ANSYS Fluent[®] codes. Finally, Sudarma et al. [40] compared the $k-\epsilon$ and Reynolds stress turbulence model in RANS simulations.

In this paper, the aforementioned burner, both in the case of CH₄–air and H₂–air mixtures, was simulated. In the case of the CH₄–air mixture, the numerical set-up was validated against experimental results [37] and benchmark CFD data [39]. Moreover, the influence of turbulence models, $k-\epsilon$, $k-\omega$ -SST, and Reynolds stress, was investigated. A study of the burner fueled with a H₂–air mixture was carried out in order to compare the flame shape with the case fueled by the CH₄–air mixture. Finally, a study of the acoustic modes (frequency and growth rates) by using an FEM approach (COMSOL Multiphysics[®]) was carried out using the two fuel mixtures in order to understand the influence of hydrogen on the thermoacoustic behaviour.

The paper is organized as follows: Section 2 describes the burner geometry, Section 3 describes the governing equations and numerical setup of the employed CFD code (ANSYS Fluent), both in the case of the burner fueled with CH₄–air and H₂–air mixtures. In the same section, the thermoacoustic model and numerical setup of the Helmholtz solver (COMSOL Multiphysics) are presented. Section 4 presents a comparison between CFD results of the two mixtures investigated in terms of velocity, temperature, density and heat release rates distributions. These CFD results were used to perform a comparison between the two mixtures in terms of the thermoacoustic analysis. Finally, Section 5 ends up the work with a sum up and the discussion of the results.

2. Combustor Geometry

In this work, a lab-scale stabilized premixed burner developed at the Vanderbilt University has been investigated. Its geometry has been retrieved by [36–40]. In Figure 1, the geometry of the whole experimental setup is displayed. Moreover, in the same figure a representation of the whole experimental setup is reported. In the same figure, a close up of the region representing the numerical domain studied in this work is shown (highlighted in the red rectangular). The rest of the geometry (grey) has been discarded in order to minimize the computational cost of the CFD simulations. As depicted in Figure 1, the burner consists of a conical stainless steel bluff body with a diameter $D = 44.45$ mm and a vertex angle of 90°. The bluff body installation is co-axial with the combustion chamber. As Pan et al. described in [36], a turbulence grid was inserted at 58 mm upstream of the bluff body. The combustion chamber shows a squared cross section (79 mm × 79 mm) with a length of 342 mm. The blockage ratio of this burner is equal to 25% (i.e., the ratio between bluff body section and the squared cross section of the inlet channel).

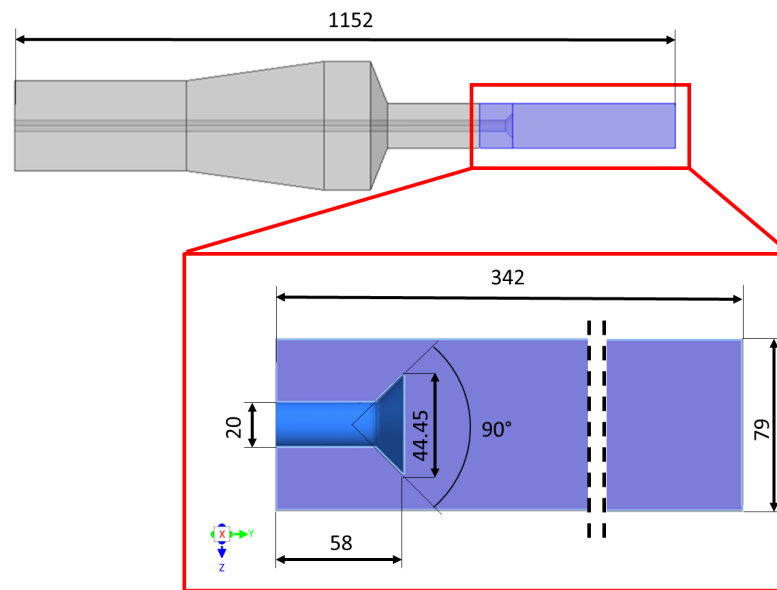


Figure 1. Representation of the numerical domain of the Vanderbilt University lab-scale burner. Dimensions are expressed in mm.

3. Governing Equation and Numerical Setup

The mathematical models of the CFD code and thermoacoustic combustion model are presented in this section. In Section 3.1, the boundary conditions, the mesh used in the CFD simulation, and the governing equations of the CFD simulations on the Vanderbilt burner are presented. Section 3.2 contains the thermoacoustic governing equations utilized to determine the stability of the system. Section 3.3 presents the boundary conditions and numerical setup for the thermoacoustic simulation of the burner powered by a mixture of pure methane or pure hydrogen.

3.1. CFD Simulations

Concerning a fully premixed flame, to model the flame front propagation, the transport equation of the progress variable, θ , which varies from 0 (fresh reactants) to 1 (burnt gases), was solved [41]. The progress variable is provided in terms of reduced fuel mass fraction, given by:

$$\theta = \frac{Y - Y_u}{Y_b - Y_u} \quad (1)$$

where Y , Y_u , and Y_b are local, unburnt, and burnt species mass fractions. The density-weighted mean reaction progress variable, represented by $\bar{\theta}$ is used to model the propagation of the flame front:

$$\frac{\partial}{\partial t}(\rho\bar{\theta}) + \nabla \cdot (\rho\mathbf{u}\bar{\theta}) = \nabla \cdot \left(\left(\frac{k}{c_p} + \frac{\mu_t}{Sc_t} \right) \nabla \bar{\theta} \right) + \rho S_c \quad (2)$$

where Sc_t is the Schmidt turbulent number and S_c is the product formation rate that represent the reaction progress source term, s^{-1} . The energy equation in terms of sensible enthalpy, h , for the fully premixed fuel is

$$\frac{\partial}{\partial t}(\rho h) + \nabla \cdot (\rho\mathbf{u}h) = \nabla \cdot \left(\frac{k + k_t}{c_p} \nabla h \right) + S_{h,chem} + S_{h,rad} \quad (3)$$

where $S_{h,rad}$ is the heat loss due to radiation and $S_{h,chem}$ represents the heat gain due to the chemical reaction:

$$S_{h,chem} = \rho S_c H_{comb} Y_{fuel} \quad (4)$$

where H_{comb} is the lower heating value of the fuel and Y_{fuel} is the fuel mass fraction of the unburnt mixture. The mean reaction rate in Equation (2) is modeled as:

$$\rho S_c = \rho_u U_t |\nabla \bar{\theta}| \quad (5)$$

where ρ_u is the density of the unburnt mixture and U_t is the turbulent flame speed. The chemical kinetic mechanism used in this work is the GRIMECH-3.0 [42], and the Zimont model has been adopted to derive the turbulent flame velocity [43]:

$$U_t = A(u')^{3/4} U_l^{1/2} \alpha_u^{-1/4} l_t^{1/4} = A u'^{(\tau_t/\tau_c)^{1/4}} \quad (6)$$

where A is the model constant, u' is the velocity fluctuation, U_l is the laminar flame speed, $\alpha_u = k/(\rho c_p)$ is the thermal diffusivity of the unburnt mixture, l_t is the turbulence length scale, $\tau_t = l_t/u'$ is the turbulence time scale, and $\tau_c = \alpha_u/U_l^2$ is the chemical time scale. The turbulence length scale is calculated as follows:

$$l_t = C_D \frac{(u')^3}{\epsilon} \quad (7)$$

where ϵ is the turbulence dissipation rate. Three turbulence models, i.e., $k-\epsilon$, $k-\omega$ -SST and Reynolds stress were employed. The main parameters, which characterize the CH₄-air or H₂-air mixtures, used for CFD simulations are summarized in Table 1. The inlet axial velocity of the fuel mixture, u_{ax} , was calculated starting from the inlet air mass flow rate, $\dot{m}_{air} = 70.78$ g/s, indicated in [37,40] and the thermal power of the burner, $P_{burner} = 120$ kW. As a result, the air-methane mixture was introduced through the inlet section with an average velocity of 10.81 m/s. A turbulence intensity of 24% was used. The operating conditions of the fuel mixture were $T = 300$ K and at atmospheric pressure. Furthermore, the surface of the chamber was treated with a non-slip wall type boundary condition. The outflow condition was applied to the outlet surface of the combustion chamber. In the same Table 1, the main parameters of the new mixture proposed for hydrogen-air combustion are reported.

Table 1. Comparison of the main parameters characterizing the two mixtures employed in this work: CH₄-air and H₂-air.

Parameter	CH ₄ -Air	H ₂ -Air
ϕ (–)	0.586	0.481
α_{st} (–)	17.20	33.9
MW_{mix} (Kg/kmol)	28.11	24.31
α (–)	29.30	70.6
\dot{m}_{air} (g/s)	70.78	70.78
\dot{m}_{fuel} (g/s)	2.42	1
ρ_{mix} (Kg/m ³)	1.14	0.99
$U_{ax,mix}$ (m/s)	10.81	12.26
LHV (MJ/Kg)	50.0	119.9
T_{ad} (K)	1641	1577

Three different unstructured meshes were generated. As shown in Figure 2, in which Mesh #3 is reported, the domain was divided into five zones to gradually increase the element size from the bluff body zone (zone 2) to the outlet zone (zone 5). The results, in terms of axial velocity and temperature, will be reported in Section 4.1.1.

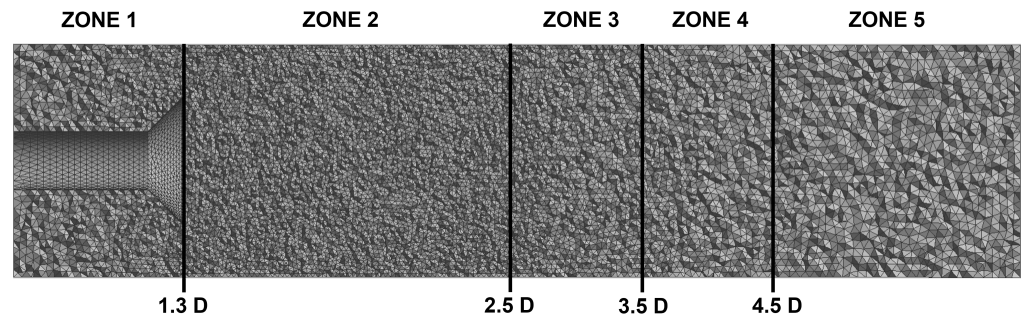


Figure 2. View of Mesh # 3 with zone partitioning for grid refinement.

3.2. Thermoacoustic Combustion Instability Modelling

Heat release and pressure fluctuations may interact to generate thermoacoustic instabilities. Instability is generated if the energy supplied is larger than the rate at which acoustic energy dissipates according to the Rayleigh criterion [44].

$$\int_0^T \int_0^V p'(x, t) q'(x, t) dv dt \geq \int_0^T \int_0^V E_d(x, t) dv dt \quad (8)$$

where p' and q' are the pressure and heat release fluctuations, respectively, T is the period of oscillation, V is the control volume, and E_d is the wave energy dissipation. According to the inequality in (8), when p' and q' are in phase instability occurs. In the combustion chambers the flow velocity is negligible with respect to the speed of sound. Under this hypothesis, the inhomogeneous wave equation in the presence of heat release fluctuations, becomes:

$$\frac{1}{\bar{c}^2} \frac{\partial^2 p'}{\partial t^2} - \nabla^2 p' = \frac{\gamma - 1}{\bar{c}^2} \frac{\partial q'}{\partial t} \quad (9)$$

where γ represents the ratio between the specific heat at constant pressure, C_p , and constant volume, C_v . The speed of sound is indicated by c and the over-bar identifies the average non-fluctuating quantity. In harmonic analysis the fluctuation of acoustic pressure p' and velocity u' are defined as follows:

$$p'(\mathbf{x}, t) = \hat{p}(\mathbf{x}) \exp(i\omega t) \quad (10)$$

$$u'(\mathbf{x}, t) = \hat{u}(\mathbf{x}) \exp(i\omega t) \quad (11)$$

where the symbol $\hat{}$ introduces a complex quantity, i is the imaginary unit, ω is the complex angular frequency, and t is time. In the case of finite disturbances, the flame model $q'(\mathbf{x}, t)$ is periodic and hence can be described by the Fourier series:

$$q'(\mathbf{x}, t) = \sum_{m=0}^{\infty} \hat{q}^m e^{im\omega t} \quad (12)$$

where m is the order of the harmonics. In this thermoacoustic analysis, neglecting non-linear and non-normal effects, we consider that the flame modes act independently from each other. Therefore, considering a single frequency:

$$\hat{q}'(\mathbf{x}, t) = \hat{q}(\mathbf{x}) e^{i\omega t} \quad (13)$$

Introducing Equations (10) and (13) into Equation (9) and considering a spatial variation of the base flow thermodynamic variables, the inhomogeneous Helmholtz Equation (14) can be derived as:

$$\frac{\lambda^2}{\bar{c}^2} \hat{p}(\mathbf{x}) - \hat{\rho}(\mathbf{x}) \nabla \cdot \left(\frac{1}{\hat{\rho}(\mathbf{x})} \nabla \hat{p}(\mathbf{x}) \right) = -\frac{\gamma - 1}{\bar{c}^2(\mathbf{x})} \lambda \hat{q}(\mathbf{x}) \quad (14)$$

where $\lambda = -i\omega$ and \mathbf{x} is the spatial coordinate. A relation that correlates the unsteady heat release rate fluctuation \hat{q} with the pressure waves is needed in order to close the thermoacoustic problem. In the frequency domain, in the case of small perturbations, the local flame response to an acoustic perturbation can be represented by the Flame Response Function (FRF). This is a complex function that depends only on the excitation or angular frequency $\omega = 2\pi f$. This function is defined as the ratio of the heat release fluctuation to the velocity fluctuation at a reference position:

$$\frac{\hat{q}(\mathbf{x})}{\bar{q}(\mathbf{x})} = FRF(\omega, \mathbf{x}) \frac{\hat{u}_j}{\bar{u}_j} \quad (15)$$

More complex model take into account the non-linear effect of the amplitude of \hat{u}_j of the acoustic velocity through a FDF (flame-describing function) depending on the acoustic velocity expressed by \hat{u}_j , not examined here. In Equation (15), the subscript j denotes the reference position. The FRF can be expressed in terms of its gain, $G = |FRF(\omega, \mathbf{x})|$, and phase, $\varphi = \arg(FRF(\omega, \mathbf{x}))$. FRF is used to define the spatial distribution of the flame response along the flame front in order to produce a more accurate response of the system than that obtained from a flame-sheet model. The evaluation of the FRF is the most important aspect of the thermoacoustic analysis because it describes the coupling between the acoustic field and the heat release fluctuations. The FRF (Equation (15)) depends on the flame characteristics, as described by Lieuwen [45] and Camporeale et al. [22]. Different physical mechanisms can be adopted in order to model the fluctuations of heat release oscillations and they are characterized by a different characteristic timescale [45]. This work is focused on the thermoacoustic instabilities occurring in a combustor equipped with a perfectly premixed burner [46]. For these kinds of combustor, the flame is fed with a premixed fuel–air stream, whose mixture is formed before entering in the burner. In perfectly premixed burners stabilized by a bluff body the driving mechanism that mostly leads to heat release fluctuations is the Flame Vortex Interaction, directly depending on the velocity fluctuation in the combustion zone. As described in [47–49] the velocity fluctuations (u') at the entrance of the combustion chamber may trigger existing “shear layer” disturbances caused by flow separation at the burner exit producing large-scale coherent vortical structures (see Figure 3). In the initial stage of their formation, these vortices generally consist of a combustible mixture. Later, as they convect towards the flame front, these vortices entrain hot combustion products and get ignited. This is followed by rapid combustion and a sudden breakdown of the vortical structures with the consequence energy transfer to lower-scale turbulence structures. If these vortical structures reach the flame front, they may distort the flame and cause its surface area to oscillate, producing fluctuations in the heat release. Figure 3 shows the recirculation zone around the bluff body for the two combinations, CH₄–air and H₂–air, that generate the vortical structures that lead to instability.

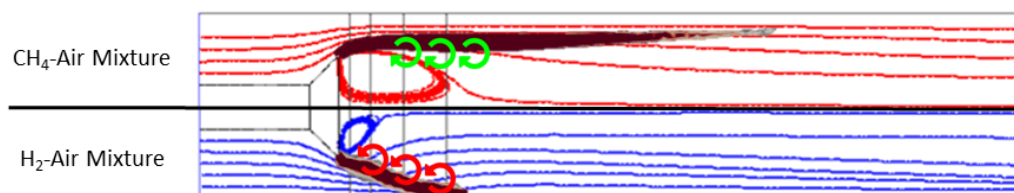


Figure 3. Schematic view of vortical structures downstream from the bluff body for the two different fuel mixtures.

The definition of the FRF model requires further attention. The FRF has been developed in several works in the literature. For instance, Durox et al. [50] studied the acoustic response of an inverted conical flame anchored on a central bluff body. In this work, the experimental campaign highlighted that the phase difference between the heat release and velocity fluctuations evolved almost linearly with frequency. In addition, Gatti et al. [51]

investigated the frequency response of three different methane–air flames. The first of them was a flame stabilized with a bluff body without swirling (as is in our case). The FRF gain curve of this flame showed typical low-pass filter behaviour with a large gain at low frequencies. For high frequencies, the FRF phase increases with constant slope. As reported in [30], in premixed combustion a mechanism contributing to the heat release rate fluctuation is the interaction of velocity perturbations, starting at the flame base, with the flame front. This process appears to be characterized, in first approximation, by a convective time delay τ (with a negligible chemical time scale). In the present work, following [27,52], this time delay was computed using a particle tracking technique. Released at $y/D = 0$, particles are tracked and a convective time computed until the flame front is reached ($Y_f = 0$). This time value, known as the “time delay”, is assigned to the position of the flame front reached by the particle. This convective delay approach appears physically sound and improves upon the one used by Alemela et al. [53], according to which the average convective delay time for premixed flames was evaluated as the ratio of the distance at which the highest reaction occurs to the effective transport velocity. With particle tracking, fluctuations of the heat release due to velocity perturbations can be more accurately tracked. Following the previous physical model, the FRF can be written as:

$$FRF = n \exp(-i\omega\tau(\mathbf{x})) \quad (16)$$

In fact, both n and τ are function of the frequency ω . The interaction index n could be modelled as a first-order low-pass filter whose cut-off frequency ω_c is defined as the angular frequency at which the gain begins to decrease [54,55]. A sensibility analysis on the interaction index and a validation on the time delay calculation will be shown in Section 4.2.2.

3.3. Thermoacoustic Numerical Setup

The thermoacoustic analysis was conducted using COMSOL Multiphysics® code as a FEM solver of the Helmholtz problem. Figure 4 depicts the numerical domain used in COMSOL.

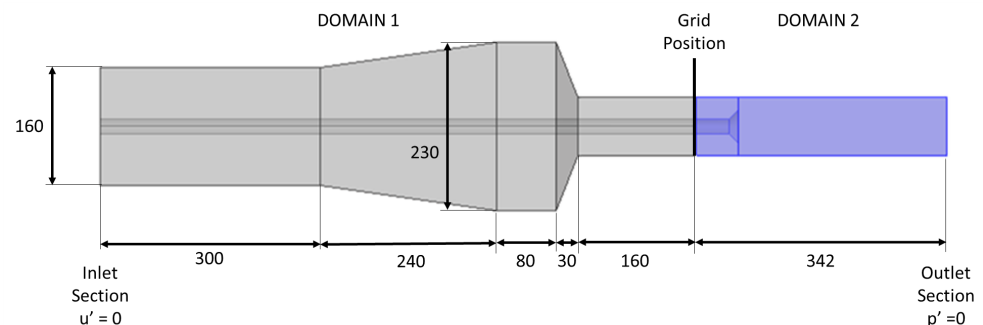


Figure 4. Numerical domain and relative boundary conditions used in the COMSOL Multiphysics®. The area in light blue represents the domain of the burner object of the aforementioned CFD simulation. Dimensions are expressed in mm.

In the experimental test-rig described in [36], a turbulence grid was inserted 58 mm upstream from the bluff body. Upstream from the turbulent grid there is a volume in which the mixture is injected. In order to account the acoustic wave propagation this volume was considered. A boundary condition of closed wall was imposed at the inlet section ($u' = 0$), while the outlet section of the combustion chamber was considered as acoustically open ($p' = 0$) considering the characteristics of the experimental setup [31].

In order to carry out the acoustic characterization of the burner, the module acoustic pressure and frequency domain of COMSOL Multiphysics® was used. COMSOL Multiphysics® solves the complete wave equation for each cell into which the 3D acoustic domain can be divided. Indicated with Q^{CM} , the monopole source:

$$Q^{\text{CM}} = -\frac{(\gamma - 1)}{\rho \bar{c}^2} \lambda \hat{q} \quad (17)$$

then the Helmholtz equation (see equation (18)), solved in COMSOL code, becomes:

$$\frac{\lambda^2}{\bar{c}^2 \bar{\rho}(\mathbf{x})} \hat{p}(\mathbf{x}) - \frac{\nabla^2 \hat{p}}{\bar{p}} = Q^{\text{CM}} \quad (18)$$

In the thermoacoustic analysis, in order to take into account the combustion process, it is necessary to transfer the results obtained from the numerical CFD simulation, carried out through ANSYS Fluent® (i.e., flame shape, reaction rate, density, temperature molecular weight and time delay), to the FEM code COMSOL Multiphysics® simulation. This procedure required the development of special Matlab code. Since the COMSOL mesh is coarse compared to the Fluent one (700 k elements of Fluent mesh with respect to 123 k elements of COMSOL mesh), the code was developed with the purpose of interpolating 3D data from Fluent to COMSOL. The Matlab code works as follows: the nodes of the two meshes are read in terms of their 3D coordinates (x , y , z). It is important to highlight that the coordinate system origins of both meshes are the same. Then, for each node of the COMSOL mesh, the code associates the thermodynamic property value of the Fluent mesh closest node. These fields were used in the monopole source defined in COMSOL.

4. Results

The outcomes of this work are presented in this section. The first part presents a sensitivity analysis of the grid and the turbulence model for the CFD simulation, followed by a comparison of the simulations of the burner fueled by pure methane and pure hydrogen mixtures. The comparison of the thermoacoustic stability between the burners fueled by the two aforementioned mixtures is shown in the second section.

4.1. Simulation of Combustion with CH_4 and H_2

4.1.1. Grid Sensitivity Analysis of the RANS Simulations

In Table 2, the zone extension along the axial distance (mentioned in Section 3.1), y , are expressed as a function of the bluff body diameter (D). Mesh #1 and #2 are characterized by a uniform grid size, i.e., 4.5 and 3 mm, respectively. On the other hand, Mesh #3 is characterized by an element size of 3 mm in zones 1 and 5 with different levels of refinement in zones 2, 3 and 4.

Table 2. Summary of the grid refinement strategy applied in this work. For each zone, the cell dimension is reported (D is the bluff body diameter).

Zone	Stream Direction	Mesh #1	Mesh #2	Mesh #3
ZONE 1	0–1.3 D	4.5 mm	3 mm	3 mm
ZONE 2	1.3 D –2.5 D	4.5 mm	3 mm	1.6 mm
ZONE 3	2.5 D –3.5 D	4.5 mm	3 mm	2 mm
ZONE 4	3.5 D –4.5 D	4.5 mm	3 mm	2.5 mm
ZONE 5	4.5 D –7.7 D	4.5 mm	3 mm	3 mm
N. of elements		200 k	700 k	2.4 M

Figure 5 shows the comparison between the axial velocity profiles at different positions y/D for the three grid refinements. The results refer to a reacting case with a methane–air mixture. All the cases were computed by using the k - ω -SST model for turbulent closure. Finally, the numerical results are in good agreement with the experiments. In conclusion, Mesh #2, with 700,000 elements, was chosen in order to retain good accuracy together with a reasonable computational cost.

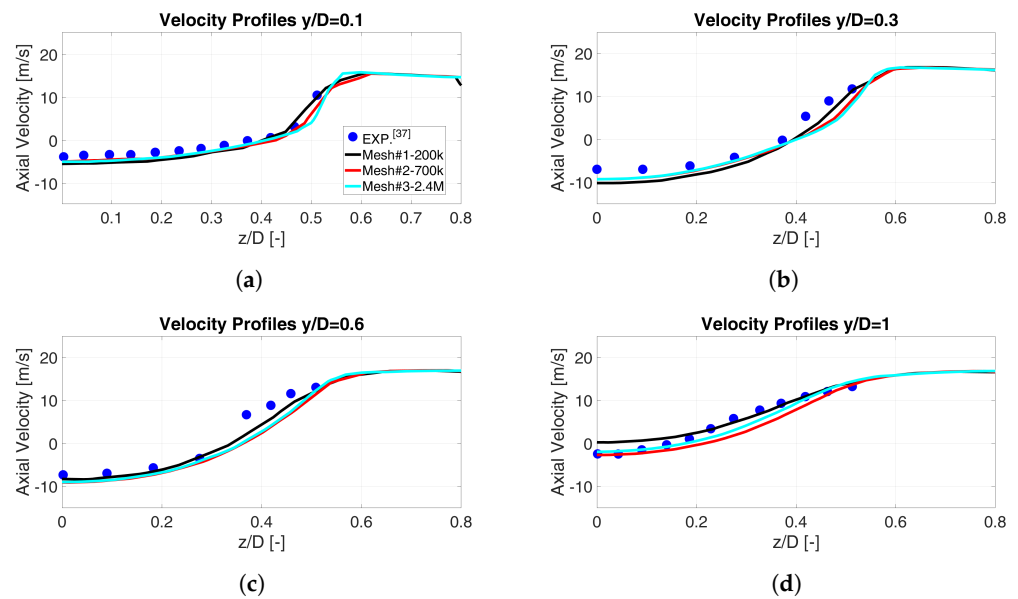


Figure 5. Mesh refinement: comparison between the experimental and the numerical results in terms of the axial velocity profiles at different axial positions ((a) $y/D = 0.1$, (b) $y/D = 0.3$, (c) $y/D = 0.6$, (d) $y/D = 1$) – reacting case.

4.1.2. Turbulence Model Sensitivity Analysis of the RANS Simulations

The Reynolds Averaged Navier Stokes (RANS) equations were solved, thus the solution is related to the integral effects of the fluctuations, also called the “turbulence effects”, on the mean flow. The closure of the momentum equations is based on the estimation of the Reynolds stresses. Several models are widely used in CFD codes. Concerning RANS simulations, the choice of the proper model should be made according to the flow characteristics. Here, the results of three different turbulence models ($k-\varepsilon$, $k-\omega$ -SST, and Reynolds Stress Model) are compared in order to select the best compromise between reliability of the solution and computational cost. The $k-\varepsilon$ model is a two-equation turbulent model used for the free shear layer away from the surfaces [56], thus expected to fail in capturing the downward recirculation of the bluff body. In order to extend the limitations of the $k-\varepsilon$ model for separate flow regions, a two-equation turbulent model $k-\omega$ SST model could be considered, where ω stands for the specific turbulence dissipation rate. Moreover, the Reynolds stress turbulence model solves the transport equations for all components of the Reynolds stress together with the dissipation rate. This leads to solve a system of seven equations in 3D flows and for this reason, the computational cost becomes very high.

The RANS numerical setup of the burner fueled with the CH_4 -air mixture was used to perform combustion analysis and to select the most suitable turbulence model that matches the experimental findings. Figure 6 shows the comparison between measured [36,37] and numerical axial velocity profiles for different axial positions (i.e., $y/D = 0.1, 0.3, 0.6$ and 1). It is possible to note the presence of an internal recirculation zone, which is due to the presence of a bluff body. When the RSM and $k-\omega$ -SST turbulence models were used, the axial velocity profiles at $y/D = 0.1$ (cyan and green line, respectively) showed good agreement with experimental data (see Figure 6a). Instead, the $k-\varepsilon$ model (red line) is unable to catch the correct flow recirculation level as demonstrated by the axial velocity profiles compared along the radial direction (z/D). Therefore, $y/D = 0.3$ and $y/D = 0.6$ (see Figure 6b,c), highlight the not physical behaviour of the numerical solution due to the $k-\varepsilon$ model. Otherwise the $k-\omega$ -SST and Reynolds stress model solutions showed similar results. Finally, at $y/D = 1.0$ the recirculation zone shrinks; thus, the flow is less affected by the turbulence model and the different solutions get closer the experimental profile (Figure 6d). In addition, the three turbulence models listed above were compared in terms of temperature (see Figure 7). The turbulence model with the best agreement with the experimental results was the $k-\omega$ -SST. In conclusion, as shown in Figures 6 and 7), the

predicted velocity profiles obtained with the $k-\omega$ -SST turbulence model and RSM better approximate the experimental results. Moreover, comparing the numerical results with the experimental ones in terms of the maximum radial length (z/D) of the recirculation zone, the $k-\epsilon$ model involves an error up to 39%, whereas RSM and $k-\omega$ SST models show the maximum error within 6%. The computational cost of the RANS simulations with the Reynolds stress model (RSM) turbulence closure is higher than with the $k-\omega$ -SST. In fact, the RSM resolves more equations with respect to the $k-\omega$ SST model because this last model is based on the resolution of only two equations regarding the turbulence kinetic energy (k) and the specific dissipation rate ω . Since these two models showed similar results in terms of the experimental velocity, the $k-\omega$ SST model was chosen because it required less simulation computation time.

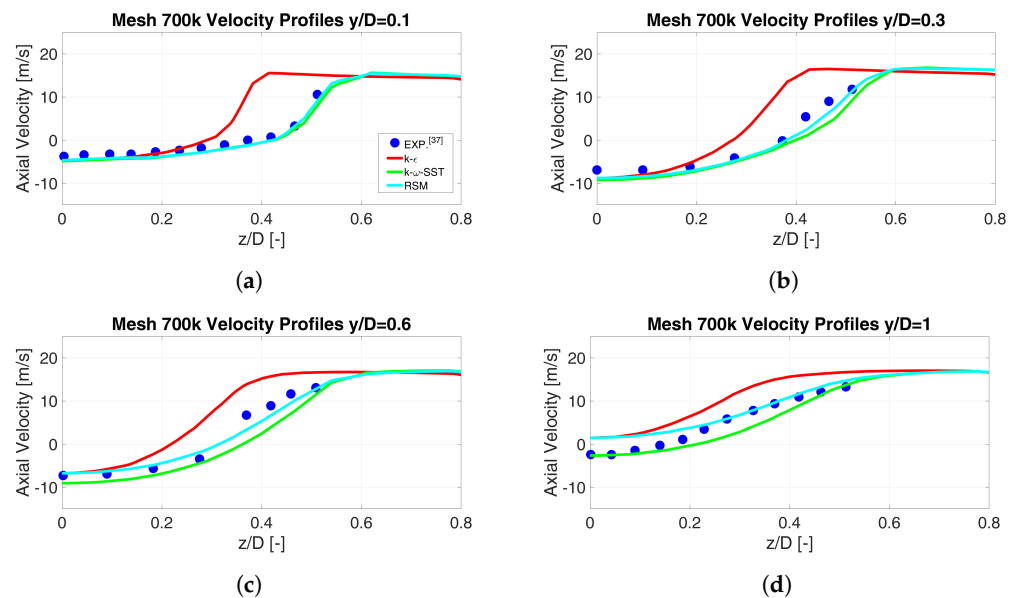


Figure 6. Study of turbulent closure: a comparison between the experimental and numerical results in terms of the axial velocity profiles for the different turbulence models ($k-\epsilon$, $k-\omega$ SST, RSM) at different axial positions ((a) $y/D = 0.1$, (b) $y/D = 0.3$, (c) $y/D = 0.6$, (d) $y/D = 1$) – reacting case.

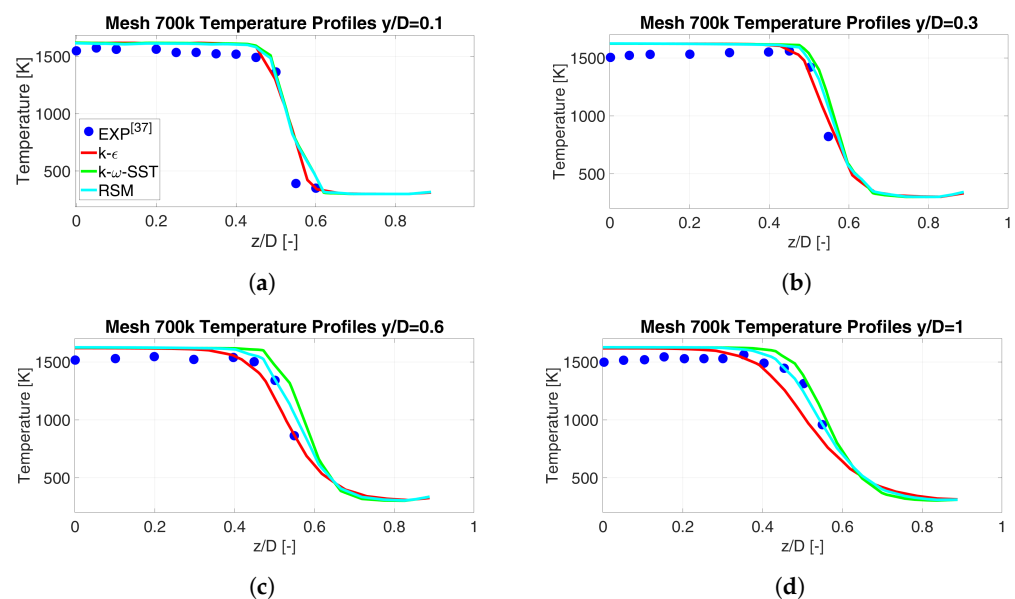


Figure 7. Study on turbulent closure: comparison between the experimental and numerical results in terms of the temperature profiles for the different turbulence models ($k-\epsilon$, $k-\omega$ SST, RSM) at different axial positions ((a) $y/D = 0.1$, (b) $y/D = 0.3$, (c) $y/D = 0.6$, (d) $y/D = 1$) – reacting case.

4.1.3. Results of the CFD Simulations

Herein, the impact of the two fuel mixtures on the performance of the burner were investigated. In particular, the 100% hydrogen case was compared to standard methane. CFD simulations were carried out to perform thermoacoustic analysis via the FEM approach. As previously presented, Table 1 compares the main parameters of the two fuel mixture compositions. The inlet axial velocity of the air–hydrogen mixture was calculated by assuming the inlet air mass flow rate, $\dot{m}_{air} = 70.78$ g/s, and the thermal power of the burner, $P_{burner} = 120$ kW as constants. As a result, the air–hydrogen mixture was introduced through the inlet section with an average velocity of 12.26 m/s, higher than the methane case.

In the first analysis a comparison between the RANS simulations of the burner fueled by methane–air mixture and the RANS simulations of the same burner developed by Andreini et al. [39] was conducted. Figure 8 shows the comparison in terms of the progress variable θ . The model developed in this work is in good agreement with respect to the RANS simulation of the burner developed by Andreini et al.

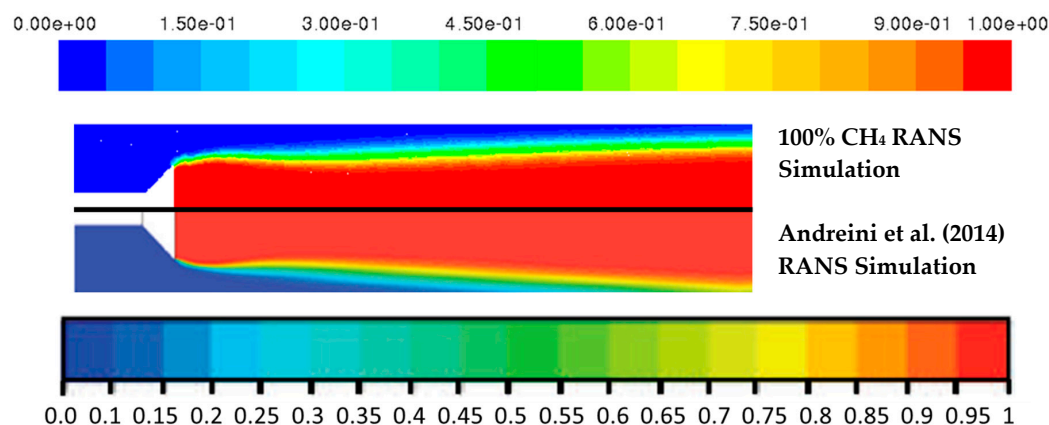


Figure 8. Comparison of the progress variable θ for a burner fueled with the methane–air mixture with respect to the RANS simulation of the burner developed by Andreini et al. [39].

After this analysis, a comparison in terms of the heat release rate (HR) distribution between the burner fueled by the CH₄–air and H₂–air mixtures was carried out. The heat release rate (J/m³s) was calculated by developing a custom field function, multiplying the point values of the reaction rate (mol/m³s) by the heating value (J/Kg) and molecular weight of the fuel (g/mol). The reaction rate was also calculated by a custom field function, multiplying the product formation rate (1/s) by the fuel concentration (mol/m³), calculated by the RANS simulation. The product formation rate (S_c), as reported in Section 3.1, was defined as the source term in the progress variable transport equation of the premixed combustion model used to model the flame propagation front. Figure 9 shows the contours of the heat release rate for the two mixtures. In detail, the H₂–air mixture shows a change in the flame topology due to the greater reactivity of hydrogen compared to methane. This is a typical effect encountered in adapting burners designed to work with methane to the new H₂–air mixture: due to the reduction in density of the fuel mixture, its axial speed increases, introducing another variation in the operating point of the burner. Furthermore, Figure 9 shows that the max value of the heat release rate of the H₂–air mixture flame is an order of magnitude greater than the CH₄–air mixture.

Figure 10 highlights the reaction zone of the combustion chamber, by the progress variable θ for the two mixtures. The shape of θ underlines the greater chemical reactivity of hydrogen–air fuel than the methane–air.

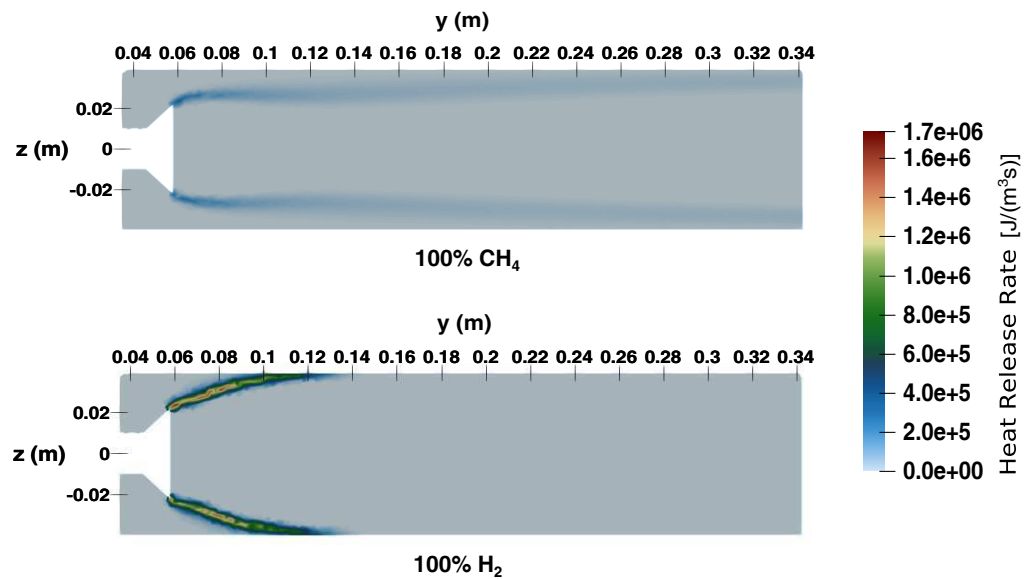


Figure 9. Contours of the heat release rate for the two different mixtures: methane–air and hydrogen–air.

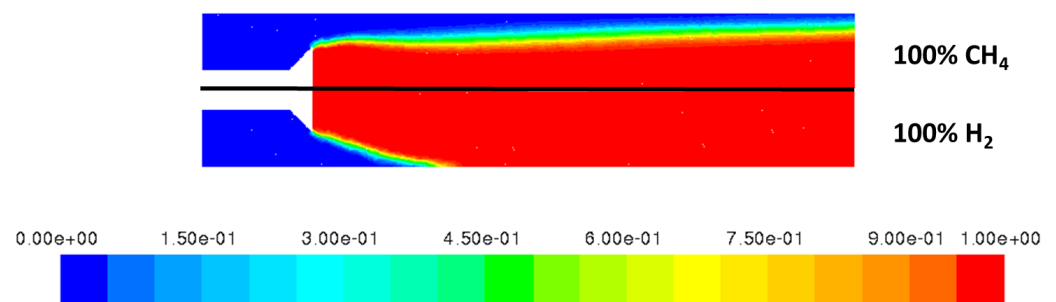


Figure 10. Contours of the progress variable θ for the two different mixtures: methane–air and hydrogen–air.

Figure 11 shows a comparison of the axial velocity profiles between the pure methane and pure hydrogen mixture combustion cases at several axial positions (i.e., $y/D = 0.1, 0.3, 0.6$ and 1). The two cases were solved by applying the $k-\omega$ SST turbulence model. At $y/D = 0.1$ (Figure 11a), the axial velocity profile for the two cases is different. Specifically, at the smallest radii until $z/D = 0.25$ the velocity of the pure hydrogen case was smaller than the benchmark. At radii higher than $z/D = 0.25$, there was a reversal trend. From the second axial position $y/D = 0.3$ (Figure 11b) the recirculation zone for the H_2 –air mixture becomes smaller with respect to the CH_4 –air mixture (the area interested in negative axial velocities reduces). At $y/D = 0.6$ and $y/D = 1$ (Figure 11c,d) concerning the H_2 –air mixture the axial velocities were positive for all coordinates z/D . Furthermore, in this case the recirculation zone becomes smaller than the CH_4 –air mixture, as it can be seen in Figure 12. The axial velocity profile variation between the two cases is due to differences in the input velocity and flame topology, which considerably modify the temperature field downstream of the bluff body (see Figure 13).

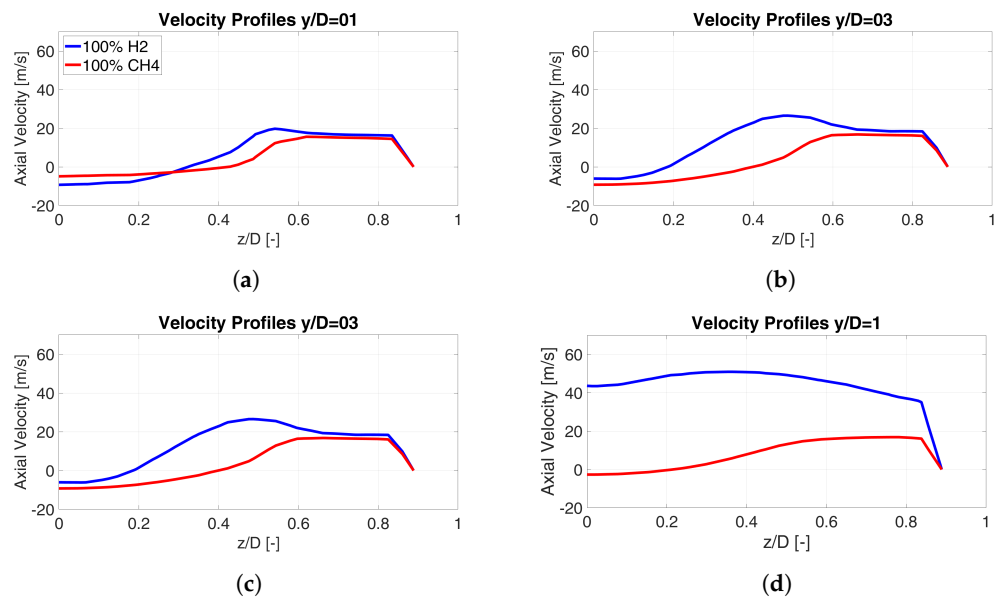


Figure 11. Comparison between the axial velocity profiles for the two different mixtures for the reaction flow, at different axial positions ((a) $y/D = 0.1$, (b) $y/D = 0.3$, (c) $y/D = 0.6$, (d) $y/D = 1$).

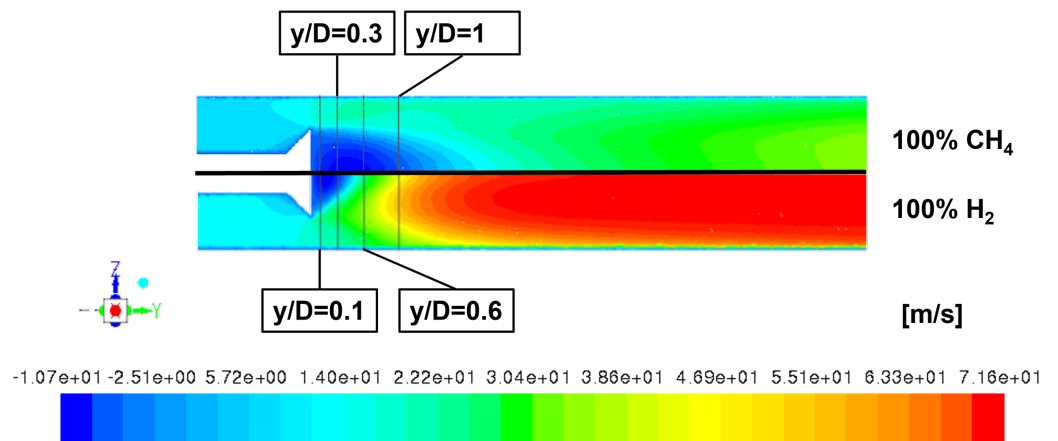


Figure 12. Comparison between the axial velocity contours for the two different mixtures. Transversal lines represent the cross-sections in which the temperature, velocity, and density profiles were measured and compared.

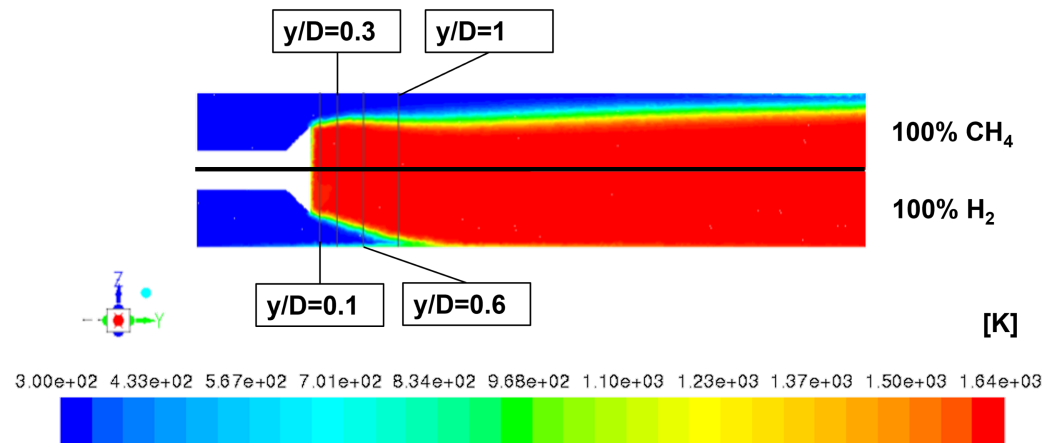


Figure 13. Comparison between the temperature contours for the two different mixtures. Transversal lines represent the cross-sections in which the temperature, velocity, and density profiles were compared.

The hydrogen flame was still anchored to the bluff body, but its different opening affects the shape of the recirculation zone. In particular, at the axial positions $y/D = 0.1$ the temperature of the two mixtures (see Figure 14a) up to the radius $z/D = 0.5$, in the case fueled by CH_4 -air mixture is equal to 1616 K, while when the fuel mixture is H_2 -air the temperature is equal to 1592 K. At the radii higher than $z/D = 0.5$, the maximum difference between the temperature of two mixtures is 4.7%. At $y/D = 0.3$ (see Figure 14b), until radius $z/D = 0.5$, the temperature of CH_4 -air mixture is constant equal to 1623 K, while in the case of H_2 -air mixture the temperature increase from 1594 K to 1614 K. After radius $z/D = 0.5$, the difference between the temperature of two mixtures increases up to 28%. The temperature of H_2 -air mixture is higher than CH_4 -air mixture at $y/D = 0.6$ and $y/D = 1$, (see Figure 14c,d).

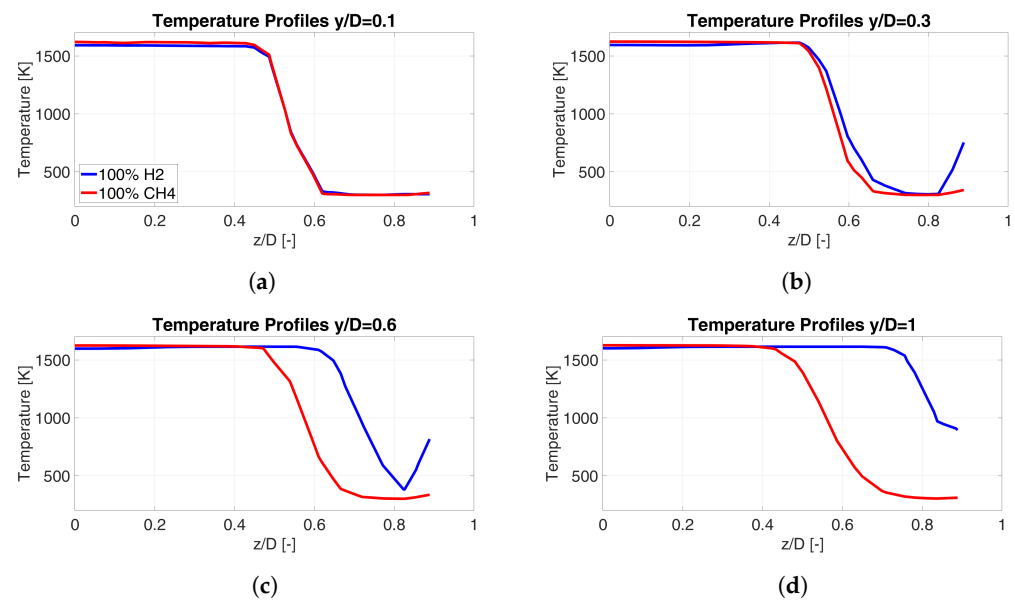


Figure 14. Comparison between the temperature profiles for the two different mixtures at different axial positions ((a) $y/D = 0.1$, (b) $y/D = 0.3$, (c) $y/D = 0.6$, (d) $y/D = 1$).

Figure 15 shows the differences between the two mixtures in terms of their density at four axial positions along the radial direction. In each section, the density of the H_2 -air mixture is less than the CH_4 -air mixture.

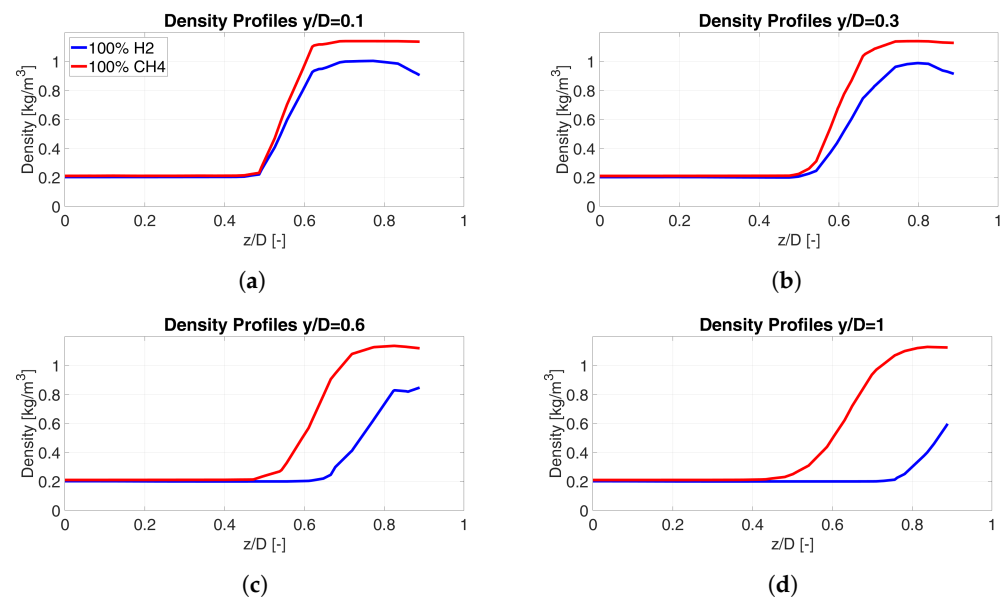


Figure 15. Comparison between the density profiles of the two different mixtures, at different axial positions ((a) $y/D = 0.1$, (b) $y/D = 0.3$, (c) $y/D = 0.6$, (d) $y/D = 1$).

4.2. Influence of Fuel on the Thermoacoustics

4.2.1. Grid Sensitivity Analysis of the Thermoacoustic Simulations

Furthermore, for the COMSOL setup, a grid sensitivity analysis was carried out. The mesh was divided in two domains, i.e., upstream (domain 1) and downstream (domain 2) of the turbulence grid. Table 3 compares three different meshes in terms of the number of elements, element sizing and computational time.

Table 3. Mesh refinement for the FEM simulations in COMSOL.

Domain	Parameter	Mesh A	Mesh B	Mesh C
Domain 1 (upstream of grid)	Max element size	92 mm	63.4 mm	40.3 mm
	Min element size	11.5 mm	4.61 mm	1.73 mm
	Max element growth rate	1.45	1.4	1.35
Domain 2 (downstream of grid)	Max element size	40.3 mm	23 mm	23 mm
	Min element size	1.73 mm	0.24 mm	0.24 mm
	Max element growth rate	1.35	1.3	1.3
Number of elements (-)		31 k	123 k	255 k
Computation time (s)		64	332	623

Moreover, a comparison between the three meshes was carried out by computing the first eigenmodes (see Figure 16). Specifically, the growth rate (GR) in this figure corresponds to the imaginary part of each eigenmodes and allows the identification of the stable ($GR < 0$) and unstable modes ($GR > 0$). The results from the grid sensitivity analysis point out the low sensitivity of the results to the grid size. The largest difference corresponded to the third frequency ($f \sim 460$ Hz) in terms of the GR. For the other points, the difference was negligible. Hence, Mesh B was chosen to be the best compromise between the reliability of the results and computational cost. On this grid, the results of the CFD simulations were transferred to perform accurate FEM analyses. In order to have good interpolation of the results from one grid (CFD–Fluent) to the other (FEM–COMSOL), Mesh B was considered equally appropriate (see Table 3). As summarized in Table 3, this mesh had a number of elements close to 123,000, a maximum element size of 63.4 mm in domain 1, and a maximum element size of 23 mm in domain 2.

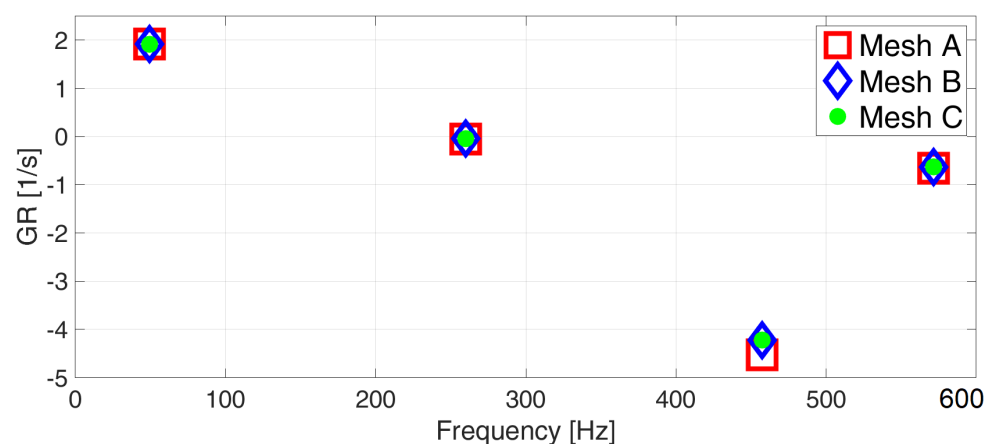


Figure 16. Comparison between the eigenmodes obtained by using different mesh refinements in COMSOL.

4.2.2. Results of the Thermoacoustic Simulations

Regarding the assumption on the n value, a sensitivity analysis on the interaction index n was carried out. In Figures 17 and 18 the frequencies and growth rate (imaginary

part of the complex frequency) are reported for the first four modes in the burner fueled with the CH₄–air and H₂–air mixtures. It can be observed that only the interaction index n influenced the absolute frequency and gain but not the mode types. In particular, the main difference between the absolute growth rate values was only reached for the first and third modes. In this work, a comparison between the burner fueled with methane–air and hydrogen–air mixture was developed by fixing the n value to equal one. This assumption was conducted to only highlight the influence of compactness on flame shape in the 100% hydrogen case. Naturally, the assumption of $n = 1$ is very strong but it is necessary to develop a sensibility analysis on the different time delays between the two mixtures.

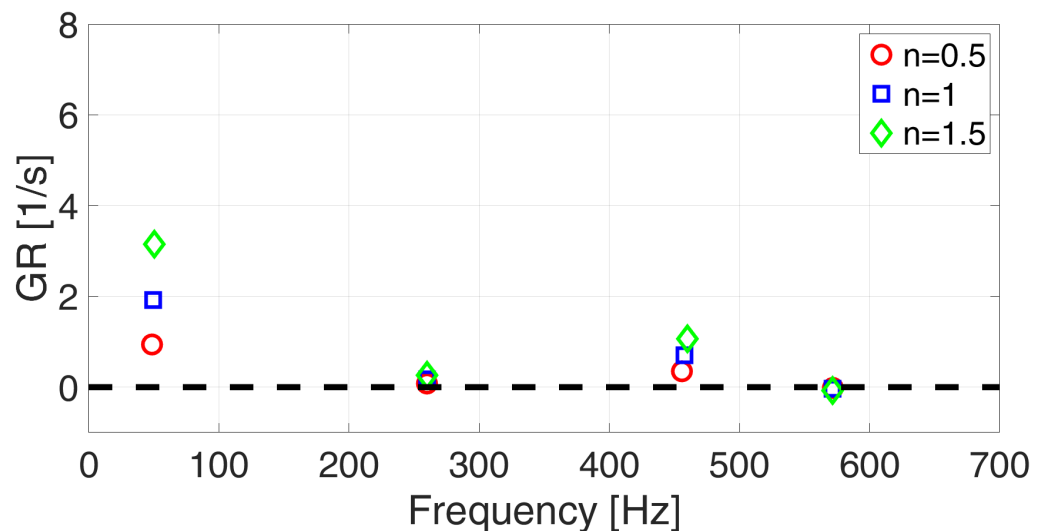


Figure 17. Sensibility analysis on the interaction index n for the benchmark CH₄–air mixture.

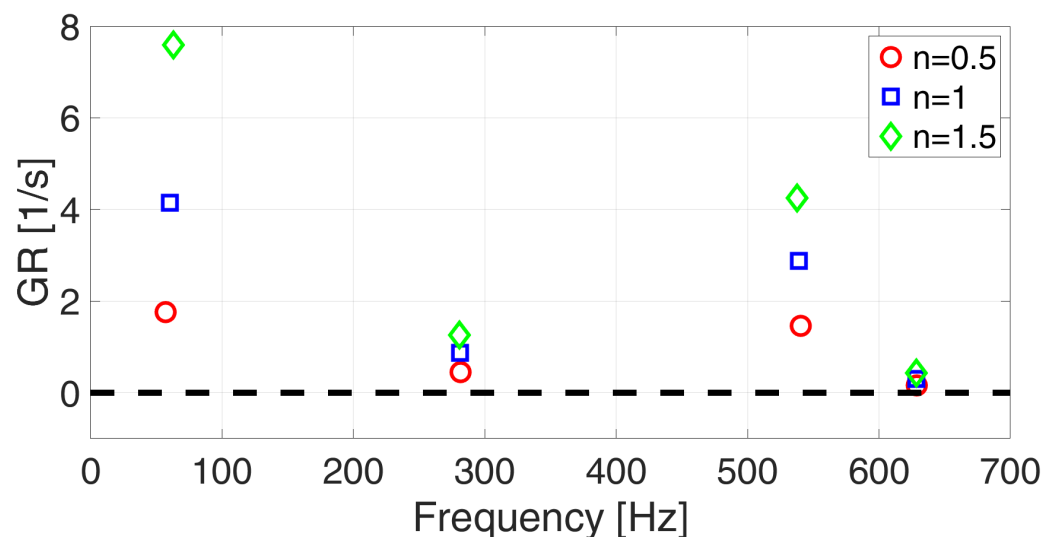


Figure 18. Sensibility analysis on the interaction index n for the H₂–air mixture.

Time delay differs from one point to another; therefore, instead of using a single time delay, a spatial distributed $\tau(\mathbf{x})$ was introduced to the model. In general, the distributed time delay is evaluated as:

$$\tau(\mathbf{x}) = \int_0^{\mathbf{x}} \|d\mathbf{s}/u\| \quad (19)$$

where u is the local spatial velocity, \mathbf{x} is the spatial coordinate of the flame front, and $d\mathbf{s}$ is the infinitesimal distance covered by points on the curvilinear trajectory. This method leads to a distributed time delay calculation with a constant time delay proposed by Æsøy et al. and Aguilar et al. [30,31]. Starting from Equation (20), where H is the flame length

and u_{bulk} is the bulk velocity, the constant time delay developed for the CH₄–air and H₂–air mixtures are equal to 0.0135 and 0.0059 s, respectively.

$$\tau = H/u_{bulk} \quad (20)$$

The values of H , shown in Figure 19, are equal to 0.188 and 0.0919 m for pure methane and pure hydrogen, respectively. The flame length was calculated as the distance between the plane $y/D = 0$ and the “centre of gravity” for the heat release rate (HRR), as reported in [31] (see Equation (21)). The values of u_{bulk} are equal to 13.67 and 15.5 m/s for the CH₄–air and H₂–air mixtures, respectively.

$$H = \frac{\int_V y \text{HRR}(x, y, z) dV}{\int_V \text{HRR}(x, y, z) dV} \quad (21)$$

Figure 19 shows the flame length H , used in Equation (20), for the two different mixtures. The red and cyan solid lines represent the flame front for pure methane and pure hydrogen, respectively. The flame front was identified by isolines corresponding to the heat release rate equal to 12.5% of the max value for methane and hydrogen.

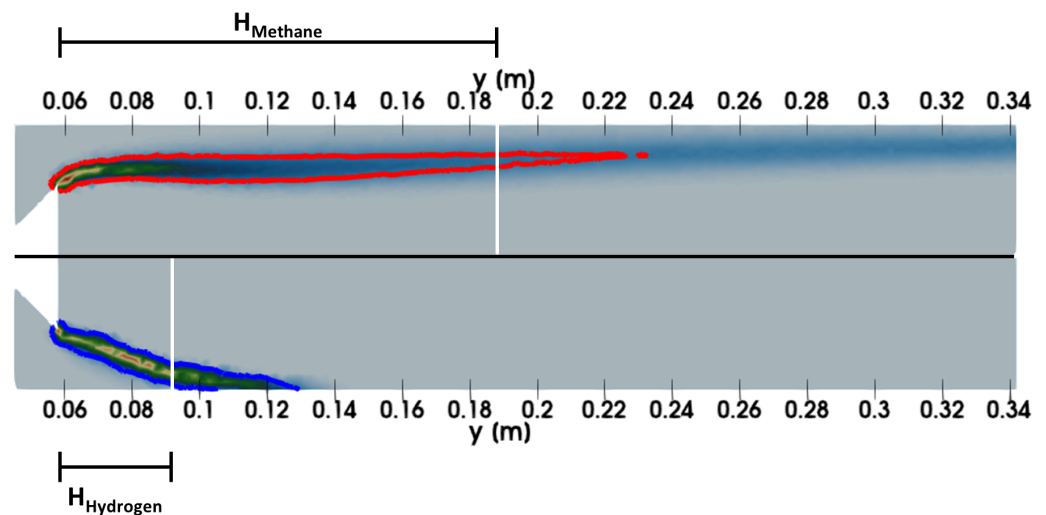


Figure 19. Schematic of the flame for the two different mixtures. The solid line denotes the flame front and H represents the length of the flame for the two mixtures.

Figure 20 shows the heat release rate against time as obtained by RANS simulations. The colours refer to different particles which are followed from the base of the flame to the flame front. The peak of the heat release rate in the burner fueled with CH₄–air (see Figure 20a) was around the time value 0.013 s. In the case of the burner fueled with H₂–air (see Figure 20b) the peak corresponds to 0.0058 s. These values, obtained by the RANS simulations, agree with respect to the constant time delay calculated by Equation (20).

In Figure 21, a scatter plot of the distributed time delay against the heat release rate (HRR) for the two mixtures is reported. The HRR was obtained by multiplying the reaction rate by LHV and the molecular weight of the fuel. The ranges of the distributed time delays were $0.005 \div 0.018$ and $0.002 \div 0.008$ s for the pure methane and pure hydrogen mixtures, respectively. The constant values computed by the formulation proposed by Æsøy and Aguilar [30,31] for both cases are within the corresponding ranges of the distributed time delay. The combustion rate of the hydrogen–air mixture in the burner was higher than the methane–air mixture due to the greater LHV of hydrogen compared to methane, see Figures 9 and 20. Therefore, the time delay of the hydrogen–air mixture is importantly lower than the methane–air mixture. These parameters are the most important in order to take into account the actual HRR in *Acoustic Pressure and Frequency Domain* of COMSOL Multiphysics®.

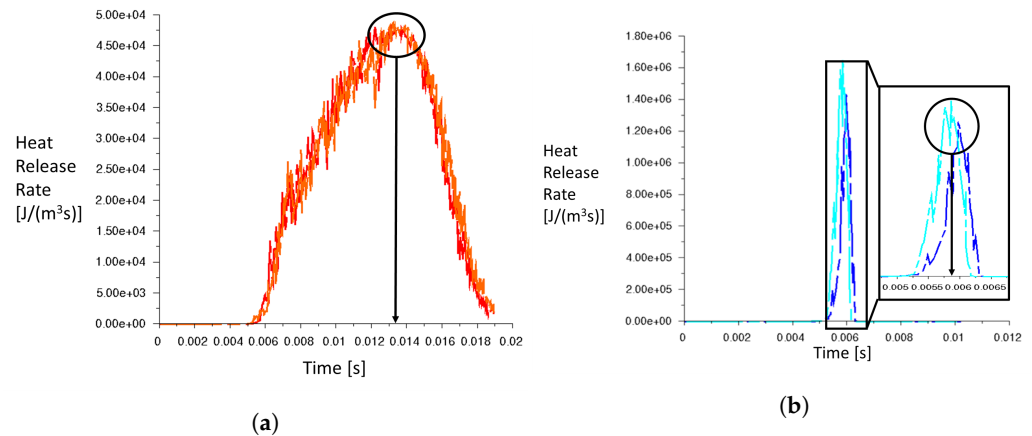


Figure 20. Heat release rate trends against time: (a) CH₄–air mixture, (b) H₂–air mixture.

In Figure 22a,b, a comparison between the temperature and the reaction rate fields of both the CFD solution (lower half section) and the data interpolated from the mesh employed on COMSOL (upper half section) is reported for the burner fueled with the CH₄–air mixture. These fields have been developed by Matlab code, aforementioned in Section 3.3. Despite the coarse mesh of FEM code, the comparison between the fields in Figure 22 shows that the results of the CFD results are well interpolated on the mesh of FEM code. This allowed us to take into account the combustion process in the thermoacoustic analysis of the burner.

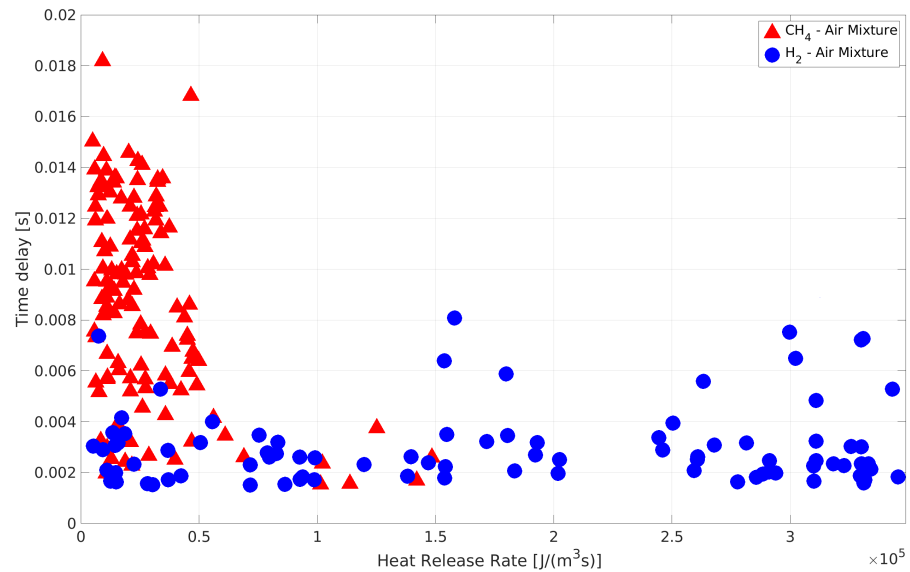


Figure 21. Comparison of the time delay versus the heat release rate for the methane–air and hydrogen–air mixtures.

The general formulation of the Rayleigh index \widehat{Ra} , in the frequency domain [57,58], is a good tool in order to individuate the region of combustion chamber in which the instability occurs. The post-processing COMSOL facilities allow to calculate the real part of Rayleigh index $Re(\widehat{Ra})$ as follows:

$$Re(\widehat{Ra}) = |\hat{p}||\hat{q}|\cos(\varphi_q - \varphi_p) \tag{22}$$

where $|\hat{p}|$ and $|\hat{q}|$ indicate the absolute value of \hat{p} and \hat{q} , respectively, φ_q is the phase of q , and φ_p is the phase of p . Figure 23 shows the contour plot of the local $Re(\widehat{Ra})$ of Equation (22) in the medium plane of the burner fueled by the CH₄–air and H₂–air mixtures. In order to perform a comparison of the results, the maximum value of $Re(\widehat{Ra})$ of the fourth mode for the two mixtures was used as the normalization factor. It is possible to notice that the shape

is very different between the two mixtures. The higher positive value of $Re(\widehat{Ra})$ obtained in the case of the H₂–air mixture (Figure 23b) confirms that the use of the hydrogen–air mixture in the burner yields an unstable mode with respect to the burner fueled with CH₄–air mixture.

In Figure 24, a distribution of the time delay τ in the burner fueled with the two mixtures is represented. When the H₂–air mixture was used the time delay τ is smaller compared to the CH₄–air mixture due to the high combustion velocity of the H₂–air fuel with respect to the CH₄–air mixture.

After studying the Rayleigh index and time delay, the next step concerns the sensibility of the burner to the different fuel mixtures. In the case of the hydrogen–air mixture the acoustic modes of the burner are reported in Figure 25. The frequencies and Growth Rate (GR) values are reported in Table 4. In the case of the burner fueled by the hydrogen–air mixture, the magnitude of the frequency and growth rate values increases with respect to the methane–air mixture. The greater reaction rate and smaller time delay of the hydrogen–air mixture stimulates a change in the relationship between the pressure fluctuation and the unsteady heat release [28]. The compactness of the flame shape in the 100% hydrogen case (see Figure 9) influences the relationship between the unsteady heat release and the pressure fluctuations and, hence, the thermoacoustic characteristics of the burner. Therefore, flame position has a crucial role in determining of the dynamic state of the burner fueled by pure hydrogen.

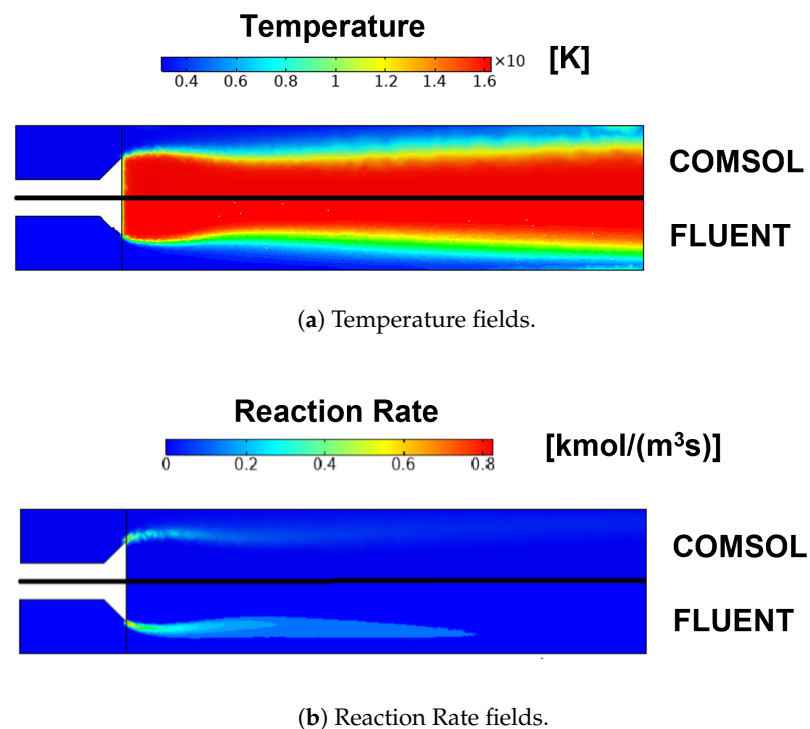
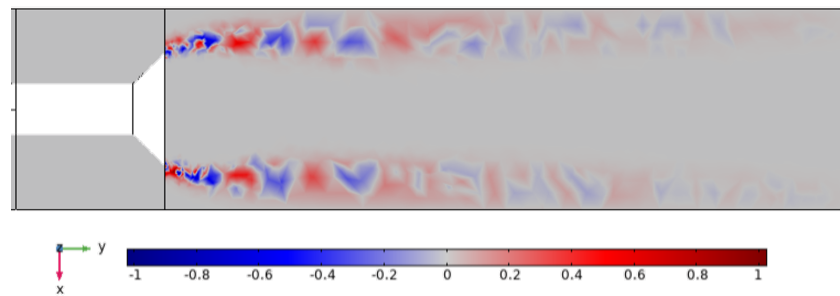
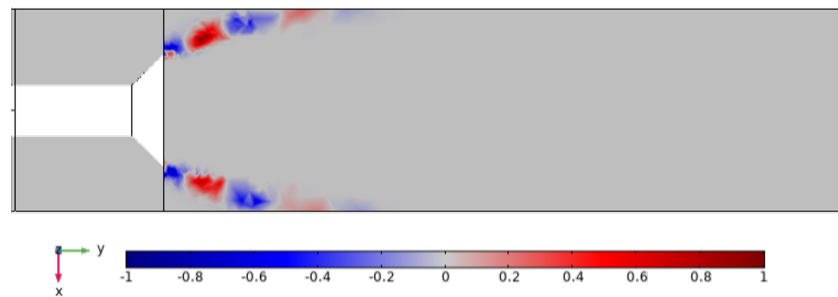
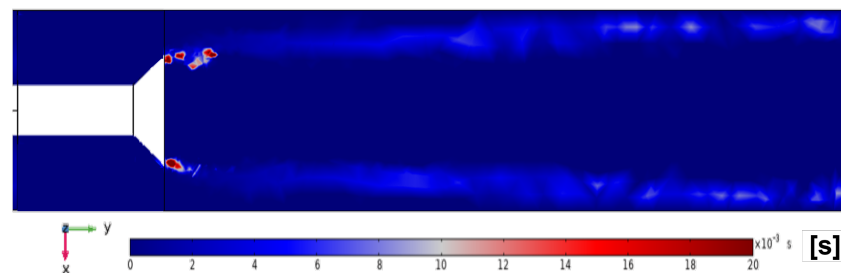
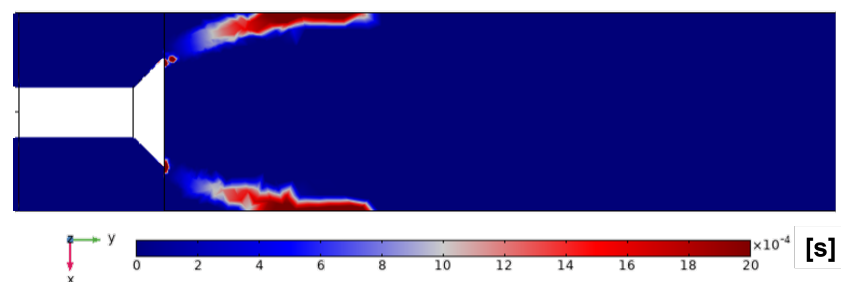


Figure 22. Comparison between the CFD solutions and the same fields interpolated on the COMSOL mesh for the burner fueled with CH₄–air mixture (Temperature field (a) and Reaction Rate field (b)).

Furthermore, in this work, due to the aforementioned causes, the thermoacoustic behaviour of the burner changes. Indeed, Figure 25 shows the increase in instability of the first two modes in the model fueled by the hydrogen–air mixture. For the same mixture, the modes at frequencies greater than 400 Hz shift towards even greater values.

(a) Rayleigh index CH₄-air mixture.(b) Rayleigh index H₂-air mixture.**Figure 23.** Comparison of the Rayleigh index for the methane–air (a) and hydrogen–air (b) mixtures.(a) Time delay CH₄-air mixture.(b) Time delay H₂-air mixture.**Figure 24.** Comparison of the time delay τ for the methane–air and hydrogen–air mixtures.

In Figure 26, the total acoustic pressure for the first four modes with the hydrogen–air and methane–air mixtures are reported. For the first two modes (Figure 26a,b), the acoustic pressure values for the hydrogen–air mixture were similar to the methane–air mixture. However, for the third mode (Figure 26c), the position of the acoustic pressure peak shifts towards the inlet section when the H₂-air mixture was used. In the fourth mode (Figure 26d), the acoustic pressure value decreases in the model of pure hydrogen compared to the CH₄-air mixture.

Table 4. Eigenmode comparisons between the H₂–air and CH₄–air mixtures.

Mode Type	CH ₄ with No Flame	CH ₄ with Flame	H ₂ with No Flame	H ₂ with Flame
Longitudinal	47.68 Hz	49.44 + 1.99i Hz	54.18 Hz	60.11 + 4.15i Hz
Longitudinal	259.73 Hz	259.96 + 0.17i Hz	281.89 Hz	281.21 + 0.87i Hz
Longitudinal	453.87 Hz	457.74 + 0.70i Hz	541.78 Hz	539.06 + 2.88i Hz
Longitudinal	571.88 Hz	571.65 – 0.038i Hz	628.95 Hz	628.48 + 0.30i Hz

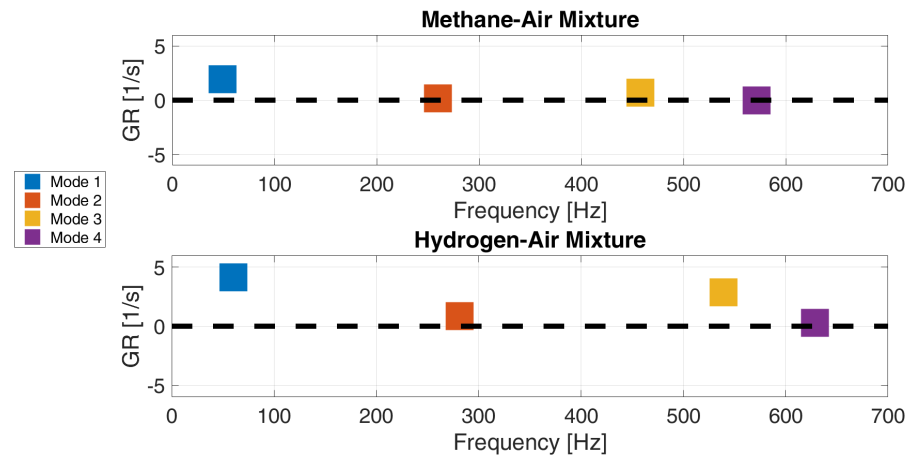


Figure 25. Comparison of the frequency and growth-rates for the two cases fueled with CH₄–air and H₂–air.

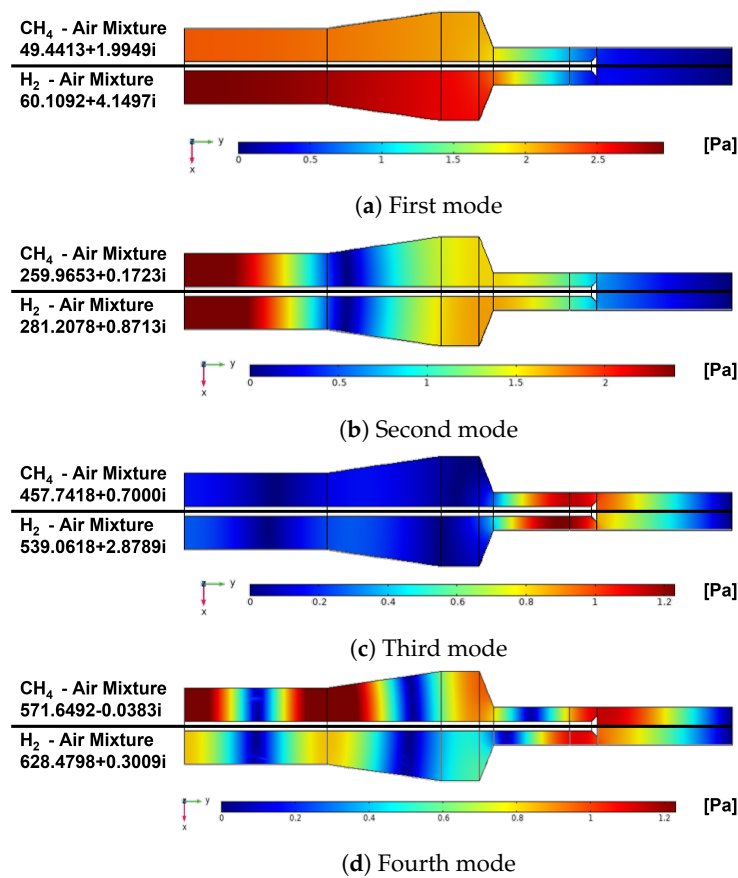


Figure 26. Comparison of the acoustic pressure for the first four modes when the two mixtures (CH₄–air and H₂–air) were employed.

5. Conclusions

In this work, the preliminary analysis of a lab-scale-stabilized burner fueled with a hydrogen–air mixture was conducted. A CFD simulation was carried out to predict the thermodynamic properties of the mixtures in the hot regions. The CFD analysis of the hydrogen–air mixture showed a reduction in the recirculation zone near the bluff body. Moreover, the data from the CFD simulations were used to develop aforementioned field proprieties and then interpolated by means Matlab code on a coarser grid used in COMSOL Multiphysics® in order to perform a thermoacoustic analysis. The time delay and heat release rate were calculated by means of the CFD simulations. In the hydrogen–air mixture case, the time delay decreased and the heat release rate increased with respect to the methane–air mixture due to the high LHV of hydrogen. A study on the Rayleigh index was carried out to analyze the influence of the H₂–air mixture on the thermoacoustic instability of the burner. Finally, an analysis of both the frequency and growth rate on the first four modes was carried out by comparing the two different mixtures. In the burner fueled by the hydrogen–air mixture, the modes were prone to becoming more unstable with respect to the same mode when fueled by the methane–air mixture due to the change in flame topology and variation in the heat release rate and time delay. In the next future, the develop of Flame Transfer Function by introducing perturbations on URANS-LES simulations will be carried out. Starting from this work, a study on the acoustic velocity fluctuation will be carried out in order to calculate the value that produces the limit cycle. The results will shed light on the main parameters affecting burner performance in the design of a new generation of hydrogen burners in the energy production sector.

Author Contributions: Conceptualization, V.C., M.S., T.C. and F.F., Methodology, V.C., M.S., T.C., F.F. and S.M.C. Formal analysis, V.C., M.S., T.C., F.F. and S.M.C., Investigation, V.C., M.S., T.C. and F.F., Data curation V.C., M.S., T.C., Writing original Draft V.C., M.S. and T.C., Writing Review & Editing, V.C., M.S., T.C. and F.F.; Supervision, S.M.C. All authors have read and agreed to the published version of the manuscript.

Funding: This research was funded by MIUR–“Ministero dell’Istruzione dell’Università e della Ricerca” under the Programmes: PON RI Research and innovation 2014-2020 CUP: D94I20000110006; Regione Puglia under the Programme: Research for Innovation (REFIN) – POR Puglia FESR FSE 2021–2020–Asse X–Azione 10.4–Codice CUP: D94I20001410008.

Data Availability Statement: Data are available upon request after emailing the authors.

Conflicts of Interest: The authors declare no conflict of interest.

Nomenclature

Subscript

<i>ax</i>	Axial component
<i>mix</i>	Fuel mix
<i>fuel</i>	Fuel
<i>j</i>	Reference position
<i>air</i>	Air
<i>st</i>	Stoichiometric
<i>burner</i>	Burner
<i>t</i>	Turbulent
<i>b</i>	Burnt
<i>u</i>	Unburnt
<i>l</i>	Laminar

Superscript

-	Mean
^	Acoustic quantity
'	Fluctuation
^m	Harmonic order

Greek letters

τ	Time delay
ω	Complex angular frequency
γ	Ratio between specific heat
ρ	Density
∂	Partial derivative
α	Fuel–air ratio
ϕ	Equivalence ratio
φ	Phase
λ	$-i\omega$
θ	Progress variable
μ	Viscosity

Symbols

n	Acoustic–combustion interaction index
D	Bluff body max diameter
D_c	Diffusion coefficient
T	Temperature
p	Pressure
u	Velocity
u_{bulk}	Bulk velocity
P	Thermal power
y	y-coordinate
z	z-coordinate
C_p	Specific heat at constant pressure
C_v	Specific heat at constant volume
q	Heat release rate
c	Speed of sound
MW	Molecular weight
V	Control volume
f	Frequency
\mathbf{x}	Spatial coordinate
Re	Real part
Ra	Rayleigh index
E_d	Wave energy dissipation
Sc	Schmidt number

Abbreviations

CFD	Computational fluid dynamics
FRF	Flame response function
RANS	Reynolds-averaged Navier–Stokes
FEM	Finite element method
GR	Growth rate
LHV	Lower heating value
FRF	Flame transfer function

References

1. Capurso, T.; Stefanizzi, M.; Torresi, M.; Camporeale, S. Perspective of the role of hydrogen in the 21st century energy transition. *Energy Convers. Manag.* **2022**, *251*, 114898. [[CrossRef](#)]
2. Kovač, A.; Paranos, M.; Marcuš, D. Hydrogen in energy transition: A review. *Int. J. Hydrogen Energy* **2021**, *46*, 10016–10035. [[CrossRef](#)]
3. International Renewable Energy Agency (IRENA). Hydrogen from Renewable Power: Technology Outlook for the Energy Transition. Abu Dhabi. 2018. Available online: <https://www.irena.org/publications/2018/sep/hydrogen-from-renewable-power> (accessed on 3 March 2023).
4. Stefanizzi, M.; Capurso, T.; Filomeno, G.; Torresi, M.; Pascazio, G. Recent Combustion Strategies in Gas Turbines for Propulsion and Power Generation toward a Zero-Emissions Future: Fuels, Burners, and Combustion Techniques. *Energies* **2021**, *14*, 6694. [[CrossRef](#)]
5. Griebel, P. Gas Turbines and Hydrogen. *Hydrogen Science and Engineering: Materials, Processes, Systems and Technology*; Wiley: Hoboken, NJ, USA, 2016; pp. 1011–1032.

6. Stefanizzi, M.; Stefanizzi, S.; Ceglie, V.; Capurso, T.; Torresi, M.; Camporeale, S.M. Analysis of the partially premixed combustion in a lab-scale swirl-stabilized burner fueled by a methane-hydrogen mixture. *E3S Web Conf.* **2021**, *312*, 11004.
7. Kutne, P. *The Path Towards a Zero-Carbon Gas Turbine*; Technical Report, European Turbine Network; ETN Global: Brussels, Belgium, 2020.
8. Guiberti, T.F.; Durox, D.; Scoufflaire, P.; Schuller, T. Impact of heat loss and hydrogen enrichment on the shape of confined swirling flames. *Proc. Combust. Inst.* **2015**, *35*, 1385–1392. [[CrossRef](#)]
9. Kelsall, G.; Troger, C. Prediction and control of combustion instabilities in industrial gas turbines. *Appl. Therm. Eng.* **2004**, *24*, 1571–1582. [[CrossRef](#)]
10. Chterev, I.; Boxx, I. Flame Topology and Combustion Instability Limits of Lean Premixed Hydrogen Enriched Flames. In Proceedings of the 27th International Colloquium on the Dynamics of Explosions and Reactive Systems (ICDERS), Beijing, China, 28 July–2 August 2019; Volume 28.
11. Chterev, I.; Boxx, I. Effect of hydrogen enrichment on the dynamics of a lean technically premixed elevated pressure flame. *Combust. Flame* **2021**, *225*, 149–159. [[CrossRef](#)]
12. Schefer, R.W.; Wicksall, D.; Agrawal, A.K. Combustion of hydrogen-enriched methane in a lean premixed swirl-stabilized burner. *Proc. Combust. Inst.* **2002**, *29*, 843–851. [[CrossRef](#)]
13. Stow, S.R.; Dowling, A.P. Low-order modelling of thermoacoustic limit cycles. In Proceedings of the Turbo Expo: Power for Land, Sea, and Air, Perugia, Italy, 14–18 June 2004; Volume 41669, pp. 775–786.
14. Evesque, S.P.; Polifke, W. Low-order acoustic modelling for annular combustors: Validation and inclusion of modal coupling. In Proceedings of the Turbo Expo: Power for Land, Sea, and Air, Amsterdam, The Netherlands, 3–6 June 2002; Volume 36061, pp. 321–331.
15. Andreini, A.; Facchini, B.; Mangani, L.; Simonetti, F. Development and validation of a 1-D tool for thermoacoustic instabilities analysis in gas turbine combustors. In Proceedings of the Turbo Expo: Power for Land, Sea, and Air, Berlin, Germany, 9–13 June 2008; Volume 43130, pp. 951–960.
16. Moin, P.; Apte, S.V. Large-eddy simulation of realistic gas turbine combustors. *AIAA J.* **2006**, *44*, 698–708. [[CrossRef](#)]
17. Boudier, G.; Gicquel, L.; Poinso, T.; Bissieres, D.; Bérat, C. Comparison of LES, RANS and experiments in an aeronautical gas turbine combustion chamber. *Proc. Combust. Inst.* **2007**, *31*, 3075–3082. [[CrossRef](#)]
18. Sengissen, A.; Van Kampen, J.; Huls, R.; Stoffels, G.G.; Kok, J.B.; Poinso, T. LES and experimental studies of cold and reacting flow in a swirled partially premixed burner with and without fuel modulation. *Combust. Flame* **2007**, *150*, 40–53. [[CrossRef](#)]
19. Staffelbach, G.; Gicquel, L.; Boudier, G.; Poinso, T. Large Eddy Simulation of self excited azimuthal modes in annular combustors. *Proc. Combust. Inst.* **2009**, *32*, 2909–2916. [[CrossRef](#)]
20. Wolf, P.; Balakrishnan, R.; Staffelbach, G.; Gicquel, L.Y.; Poinso, T. Using LES to study reacting flows and instabilities in annular combustion chambers. *Flow Turbul. Combust.* **2012**, *88*, 191–206. [[CrossRef](#)]
21. Nicoud, F.; Benoit, L.; Sensiau, C.; Poinso, T. Acoustic modes in combustors with complex impedances and multidimensional active flames. *AIAA J.* **2007**, *45*, 426–441. [[CrossRef](#)]
22. Camporeale, S.; Fortunato, B.; Campa, G. A finite element method for three-dimensional analysis of thermo-acoustic combustion instability. *J. Eng. Gas Turbines Power* **2011**, *133*, 011506. [[CrossRef](#)]
23. Laera, D.; Camporeale, S.M. A weakly nonlinear approach based on a distributed flame describing function to study the combustion dynamics of a full-scale lean-premixed swirled burner. *J. Eng. Gas Turbines Power* **2017**, *139*, 091501. [[CrossRef](#)]
24. Ceglie, V.; Capurso, T.; Oresta, P.; Camporeale, S.M. Analysis of the Influence of the Mean Flow Field Mach Number on Thermo-Acoustic Combustion Instability. *Edp Sci.* **2020**, *197*, 11004. [[CrossRef](#)]
25. Laera, D.; Agostinelli, P.W.; Selle, L.; Cazères, Q.; Öztarlık, G.; Schuller, T.; Gicquel, L.; Poinso, T. Stabilization mechanisms of CH₄ premixed swirled flame enriched with a non-premixed hydrogen injection. *Proc. Combust. Inst.* **2021**, *38*, 6355–6363. [[CrossRef](#)]
26. Crocco, L.; Cheng, S.I. *Theory of Combustion Instability in Liquid Propellant Rocket Motors*; Technical Report; Princeton University: Princeton, NJ, USA, 1956.
27. Laera, D.; Camporeale, S.M. Numerical and experimental studies on self sustained thermo-acoustic combustion instabilities of an experimental rig for full-scale industrial burners. *Int. J. Gas Turbine, Propuls. Power Syst.* **2017**, *9*, 37–46.
28. Beita, J.; Talibi, M.; Sadasivuni, S.; Balachandran, R. Thermoacoustic Instability Considerations for High Hydrogen Combustion in Lean Premixed Gas Turbine Combustors: A Review. *Hydrogen* **2021**, *2*, 33–57. [[CrossRef](#)]
29. Janus, M.C.; Richards, G.A.; Yip, M.J.; Robey, E.H. Effects of ambient conditions and fuel composition on combustion stability. In Proceedings of the Turbo Expo: Power for Land, Sea, and Air, Orlando, FL, USA, 2–5 June 1997; American Society of Mechanical Engineers: New York, NY, USA, 1997; Volume 78699, p. V002T06A035.
30. Æsøy, E.; Aguilar, J.G.; Wiseman, S.; Bothien, M.R.; Worth, N.A.; Dawson, J.R. Scaling and prediction of transfer functions in lean premixed H₂/CH₄-flames. *Combust. Flame* **2020**, *215*, 269–282. [[CrossRef](#)]
31. Aguilar, J.G.; Æsøy, E.; Dawson, J.R. The influence of hydrogen on the stability of a perfectly premixed combustor. *Combust. Flame* **2022**, *245*, 112323. [[CrossRef](#)]
32. Shanbhogue, S.; Sanusi, Y.; Taamallah, S.; Habib, M.; Mokheimer, E.; Ghoniem, A. Flame macrostructures, combustion instability and extinction strain scaling in swirl-stabilized premixed CH₄/H₂ combustion. *Combust. Flame* **2016**, *163*, 494–507. [[CrossRef](#)]

33. Ahn, B.; Indlekofer, T.; Dawson, J.; Worth, N. Transient Thermo-Acoustic Responses of Methane/Hydrogen Flames in a Pressurized Annular Combustor. *J. Eng. Gas Turbines Power* **2022**, *144*, 14. [CrossRef]
34. Veiga-López, F.; Martínez-Ruiz, D.; Kuznetsov, M.; Sánchez-Sanz, M. Thermoacoustic analysis of lean H₂-air premixed flames in thin layers. In Proceedings of the 27th International Colloquium on the Dynamics of Explosions and Reactive Systems (ICDERS 2019), Beijing, China, 28 July–2 August 2019.
35. Kim, Y.J.; Yoon, Y.; Lee, M.C. On the observation of high-order, multi-mode, thermo-acoustic combustion instability in a model gas turbine combustor firing hydrogen containing syngases. *Int. J. Hydrogen Energy* **2019**, *44*, 11111–11120. [CrossRef]
36. Pan, J.; Vangsness, M.; Ballal, D. Aerodynamics of bluff-body stabilized confined turbulent premixed flames. *J. Eng. Gas Turbines Power* **1992**, *114*, 783–789. [CrossRef]
37. Nandula, S.; Pitz, R.; Barlow, R.; Fiechtner, G. Rayleigh/Raman/LIF measurements in a turbulent lean premixed combustor. In Proceedings of the 34th Aerospace Sciences Meeting and Exhibit, Reno, NV, USA, 15–18 January 1996; p. 937.
38. Cannon, S.; Brewster, B.; Smoot, L. PDF modeling of lean premixed combustion using in situ tabulated chemistry. *Combust. Flame* **1999**, *119*, 233–252. [CrossRef]
39. Andreini, A.; Bianchini, C.; Innocenti, A. Large eddy simulation of a bluff body stabilized lean premixed flame. *J. Combust.* **2014**, *2014*, 710254. [CrossRef]
40. Sudarma, A. RANS numerical simulation of lean premixed bluff body stabilized combustor: Comparison of turbulence models. *J. Therm. Eng.* **2017**, *3*, 1561–1573. [CrossRef]
41. *Ansys Fluent Theory Guide*; ANSYS, Inc.: Canonsburg, PA, USA, 2022. Available online: <http://www.pmt.usp.br/academico/martoran/notasmodelosgrad/ANSYS%20Fluent%20Theory%20Guide%202015.pdf> (accessed on 3 March 2023).
42. Smith, G.P. GRI-Mech 3.0. 1999. Available online: <http://combustion.berkeley.edu/gri-mech/version30/text30.html> (accessed on 3 March 2023).
43. Zimont, V.; Polifke, W.; Bettelini, M.; Wolfgang, W. An efficient computational model for premixed turbulent combustion at high Reynolds numbers based on a turbulent flame speed closure. *J. Eng. Gas Turbines Power* **1998**, *120*, 526–532. [CrossRef]
44. Rayleigh, J.W.S.B. *The Theory of Sound*; Macmillan & Company: New York, NY, USA, 1896; Volume 2.
45. Lieuwen, T.C.; Yang, V. *Combustion Instabilities in Gas Turbine Engines: Operational Experience, Fundamental Mechanisms, and Modeling*; American Institute of Aeronautics and Astronautics: Reston, VA, USA, 2005.
46. Hermeth, S.; Staffelbach, G.; Gicquel, L.Y.; Anisimov, V.; Cirigliano, C.; Poinso, T. Bistable swirled flames and influence on flame transfer functions. *Combust. Flame* **2014**, *161*, 184–196. [CrossRef]
47. Schadow, K.; Gutmark, E. Combustion instability related to vortex shedding in dump combustors and their passive control. *Prog. Energy Combust. Sci.* **1992**, *18*, 117–132. [CrossRef]
48. Poinso, T.J.; Troune, A.C.; Veynante, D.P.; Candel, S.M.; Esposito, E.J. Vortex-driven acoustically coupled combustion instabilities. *J. Fluid Mech.* **1987**, *177*, 265–292. [CrossRef]
49. Matveev, K.I.; Culick, F. A model for combustion instability involving vortex shedding. *Combust. Sci. Technol.* **2003**, *175*, 1059–1083. [CrossRef]
50. Durox, D.; Schuller, T.; Candel, S. Combustion dynamics of inverted conical flames. *Proc. Combust. Inst.* **2005**, *30*, 1717–1724. [CrossRef]
51. Gatti, M.; Gaudron, R.; Mirat, C.; Zimmer, L.; Schuller, T. Impact of swirl and bluff-body on the transfer function of premixed flames. *Proc. Combust. Inst.* **2019**, *37*, 5197–5204. [CrossRef]
52. Campa, G.; Camporeale, S.M. Prediction of the thermoacoustic combustion instabilities in practical annular combustors. *J. Eng. Gas Turbines Power* **2014**, *136*, 091504. [CrossRef]
53. Alemela, P.; Fanaca, D.; Hirsch, C.; Sattelmayer, T.; Schuermans, B. Determination and scaling of thermo acoustic characteristics of premixed flames. *Int. J. Spray Combust. Dyn.* **2010**, *2*, 169–198. [CrossRef]
54. Dowling, A.P. Nonlinear self-excited oscillations of a ducted flame. *J. Fluid Mech.* **1997**, *346*, 271–290. [CrossRef]
55. Li, J.; Morgans, A.S. Time domain simulations of nonlinear thermoacoustic behaviour in a simple combustor using a wave-based approach. *J. Sound Vib.* **2015**, *346*, 345–360. [CrossRef]
56. Menter, F.R. Two-equation eddy-viscosity turbulence models for engineering applications. *AIAA J.* **1994**, *32*, 1598–1605. [CrossRef]
57. Lo Schiavo, E.; Laera, D.; Riber, E.; Gicquel, L.; Poinso, T. On the impact of fuel injection angle in Euler–Lagrange large eddy simulations of swirling spray flames exhibiting thermoacoustic instabilities. *Combust. Flame* **2021**, *227*, 359–370. [CrossRef]
58. Magri, L.; Juniper, M.P.; Moeck, J.P. Sensitivity of the Rayleigh criterion in thermoacoustics. *J. Fluid Mech.* **2020**, *882*, R1. [CrossRef]

Disclaimer/Publisher’s Note: The statements, opinions and data contained in all publications are solely those of the individual author(s) and contributor(s) and not of MDPI and/or the editor(s). MDPI and/or the editor(s) disclaim responsibility for any injury to people or property resulting from any ideas, methods, instructions or products referred to in the content.